Discovering the Solid-State Secrets of Lorlatinib by NMR Crystallography: To Hydrogen Bond or Not to Hydrogen Bond

Zainab Rehman,[a] W. Trent Franks,[a] Bao Nguyen,[b] Heather Frericks Schmidt,[b] Garry Scrivens,[c] and Steven P. Brown[a]

[a] Department of Physics, University of Warwick, Coventry, CV4 7AL, UK.
[b] Pfizer Worldwide R&D, Groton, CT, USA.
[c] Pfizer Worldwide R&D, Sandwich, Kent, UK.

Abstract

Lorlatinib is an active pharmaceutical ingredient (API) used in the treatment of lung cancer. Here, an NMR crystallography analysis is presented whereby the single-crystal X-ray diffraction structure (CSD: 2205098) determination is complemented by multinuclear (^{1}H, ^{13}C, ^{14}/^{15}N, ^{19}F) magic-angle spinning (MAS) solid-state NMR and gauge-including projector augmented wave (GIPAW) calculation of NMR chemical shifts. Lorlatinib crystallises in the $P2_1$ space group, with two distinct molecules in the asymmetric unit cell, $Z' = 2$. Three of the four NH_2 hydrogen atoms form intermolecular hydrogen bonds, N30-H…N15 between the two distinct molecules and N30-H…O2 between two equivalent molecules. This is reflected in one of the NH_2 ^{1}H chemical shifts being significantly lower, 4.0 ppm compared to 7.0 ppm. Two-dimensional ^{1}H-^{13}C, ^{14}N-^{1}H and ^{1}H (double-quantum, DQ)-^{1}H (single-quantum, SQ) MAS NMR spectra are presented. The ^{1}H resonances are assigned and specific H-H proximities corresponding to the observed DQ peaks are identified. The resolution enhancement at a ^{1}H Larmor frequency of 1 GHz as compared to 500 or 600 MHz is demonstrated.

1. Introduction

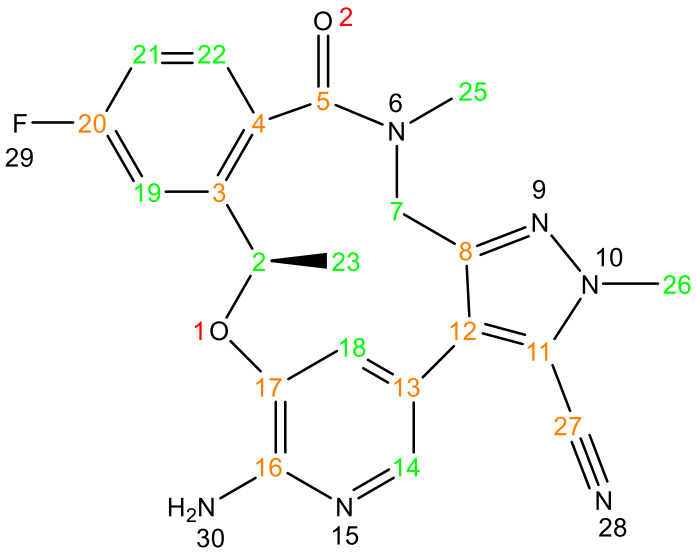

1

Lorlatinib (Lorbrena) **1**, is an oral active pharmaceutical ingredient (API) developed by Pfizer and used in the treatment, as an inhibitor, of anaplastic lymphoma kinase (ALK) and C-ros oncogene (ROS1) kinase for patients with ALK-positive or ROS1-positive non-small cell lung cancer (NSCLC).[1,2] Since receiving its first global approval in 2018 in Japan,[1] it is now widely prescribed around the world. The molecule was developed to treat patients that have developed resistance to existing therapies for ALK-positive tumours by generating a macrocyclic compound.[2] A structure-based drug design approach was implemented in order to prepare the desired macrocyclic structure, functioning as a highly potent ALK inhibitor with good absorption, distribution, metabolism and excretion.[3] Both the phase one and two trials findings indicated that the use of Lorlatinib was an effective therapeutic strategy for ALK-positive NSCLC for patients who previously showed resistance to other forms of treatment.[4,5] Lorlatinib has been recognised as a 2021 ACS 'Hero of Chemistry'.[6,7]

While a crystal structure of the HCl salt of Lorlatinib has previously been reported (CSD ZOJLIV)[3], it is the free form that is present in Lorbrena tablets.[8] This paper presents a single-crystal X-ray diffraction structure (CSD: 2205098) determination for this free form of Lorlatinib. This is complemented by a nuclear magnetic resonance (NMR) crystallography analysis that combines experimental magic-angle spinning (MAS) with density-functional theory (DFT)-based calculation of NMR parameters. We note that Ou et al[9] have reported a crystal structure of Lorlatinib (CSD: 1987322), as one of 20 clinical drugs, in a paper describing a method for

cultivating single crystals from melt microdroplets. However, this crystal structure is for racemic Lorlatinib, not the R enantiomer as in the pharmaceutical formulation.

MAS NMR is being increasingly applied to the characterisation of APIs in the solid state.[10-12] In particular, these applications benefit from recent technical advances with regards to ever faster MAS frequencies.[13-15] In particular, this benefits the application of ^{1}H detected MAS NMR, notably two-dimensional homonuclear and heteronuclear experiments, to small and moderately sized molecules such as pharmaceuticals. A key experiment is the ^{1}H-^{1}H Double Quantum (DQ) MAS NMR experiment,[16,17] in which specific ^{1}H-^{1}H proximities are observed via the homonuclear recoupling of ^{1}H-^{1}H dipolar couplings, for example using the Back-to-Back (BaBa)[18,19] pulse sequence. Powerful insight, notably into key hydrogen-bonding interactions, is obtained by combining the homonuclear ^{1}H–^{1}H DQ MAS NMR experiment with fast MAS heteronuclear experiments, specifically ^{1}H-^{13}C CP HETCOR[20-24] and ^{14}N–^{1}H heteronuclear multiple-quantum correlation (HMQC).[25-28]

In this context, it is informative to give an overview of applications of MAS NMR to pharmaceuticals and related self-assembled moderately sized organic molecules. ^{1}H–^{13}C CP HETCOR experiments have been applied to complex CO_2-based organic framework materials,[29] nanocrystals[30] and salt forms,[31] as well as to provide constraints to enhance crystal structure prediction.[32] The ^{1}H–^{1}H DQ MAS NMR experiment has found application to a cysteine-based formulation,[33] the diethylcarbamazine citrate salt which is used in the treatment of filariasis caused by worm infection,[34] the multiple-sclerosis treatment teriflunomide,[35] as well as for identifying differences between crystalline and amorphous indomethacin.[36] Other applications include ^{15}N-labelled rosette nanotubes,[37] co-crystals formed by ball milling[38] and quartet and ribbon-like self-assemblies.[39] Aromatic pi-pi interactions can also be probed by the ^{1}H–^{1}H DQ MAS NMR experiment, for example in diphenylalanine nanotubes.[40] In related pulse sequence development, it has been shown that excipient signals can be edited out of ^{1}H MAS NMR spectra of drug formulations using selective saturation pulses,[41] while a selective DQ recoupling pulse sequence has also been applied to desmotropic forms of albendazole.[42] The ^{14}N–^{1}H HMQC experiment has been applied, for example, to amorphous solid dispersions of an API,[43] paclitaxel loaded polymer micelles[44] and for probing the tautomeric form of azo dyes.[45] For fluorinated drug molecules, ^{1}H-^{19}F heteronuclear correlation

experiments can be performed, for example for the antiemetic aprepitant and its formulation[46] Emend as well as a range of blockbuster drugs.[47]

As exemplified in this paper, insight into solid-state forms of an API is obtained by applying an NMR crystallography approach.[48-55] Specifically, experimental solid-state NMR data is combined with the calculation of NMR parameters, notably, as in this study, using the DFT-based gauge-including projector augmented wave (GIPAW) approach[56,57] that is applicable to periodically repeating crystalline solids. As is the case for the solid-state structure of Lorlatinib studied here, the number of molecules in the asymmetric unit cell (*Z'*) can be greater than one. This is readily identified by an NMR crystallography approach, whereby the number of peaks per atom site can be counted, notably in a ^{13}C cross-polarisation (CP) MAS spectrum.[50,51] A recent example for a pharmaceutical salt shows how specific packing effects can be understood in this way.[58] In further examples of applying NMR crystallography to pharmaceuticals, solid-state NMR can probe proton transfer that distinguishes co-crystal or salt formation[59-62] and test the validity of structures determined by powder X-ray diffraction.[63] Moreover, a GIPAW-trained machine learning approach for the prediction of chemical shifts, ShiftML, has recently been presented.[64-66] This enabled the characterisation of an amorphous drug,[67] taking advantage of the marked sensitivity of NMR chemical shifts to local structure.[68]

In this paper, a multinuclear ^{1}H, ^{13}C, $^{14/15}N$ and ^{19}F solid-state NMR analysis incorporating two-dimensional ^{1}H-^{1}H DQ MAS, ^{1}H-^{13}C CP HETCOR and ^{14}N-^{1}H HMQC experiments at 60 kHz MAS and a ^{1}H Larmor frequency of up to 1 GHz are presented for the API Lorlatinib in its crystalline form. In an NMR crystallography approach that combines solid-state NMR experiment with GIPAW calculation, the solid-state packing in the as-reported X-ray diffraction crystal structure is explored. In particular, differences in hydrogen bonding exhibited by the NH_2 protons are quantified via large variations in their ^{1}H chemical shift.

2. Experimental

2.1 Sample Preparation

Lorlatinib was supplied by Pfizer. Material was prepared according the procedure listed in patent US 10420749.[69]

2.2 Single-Crystal X-ray Diffraction

The single crystal X-ray structure of Lorlatinib was determined at 100 K in the monoclinic system, space group $P2_1$. Data collection was performed on an Agilent SuperNova diffractometer using a CuKα X-ray source. 76328 reflections were collected using the omega collection method. The structure was solved using the SHELXTL program[70] and full-matrix least-squares refinement on F^2. All non-hydrogen atoms were refined anisotropically. All carbon-bound hydrogens were placed in geometrically calculated positions and refined using a riding model. Hydrogens atoms on heteroatoms were refined with isotropic displacement parameters. The final R-index is 4.22%. The absolute stereochemistry was determined with a Flank parameter of 0.05(4). Structural diagrams in this paper were created using Mercury 4.2.0.[71]

2.3 Solution-State NMR

Approximately 15 mg of Lorlatinib was dissolved in 0.6 mL of 99.9% deuterated dimethyl sulfoxide (DMSO-d6) with 0.05% (v/v) tetramethylsilane (TMS). Both proton and carbon dimensions were referenced using the TMS, set equal to 0.00 ppm. ^{1}H COSY, NOESY, ROESY, multiplicity-edited HSQC, HMBC, and ^{13}C nuclear magnetic resonance (NMR) spectra were acquired at 298 K using a Bruker-Biospin 5 mm TCI cryoprobe on a Bruker-Biospin AVANCE III NMR spectrometer operating at 600.0 MHz and 150.9 MHz for ^{1}H and ^{13}C, respectively.

2.4 Solid-State NMR

Experiments were performed using a Bruker AVANCE III (Warwick and Pfizer), a Bruker AVANCE II+, and a Bruker AVANCE Neo spectrometer operating at a ^{1}H Larmor frequency of 500.1 MHz, 599.5 MHz, and 1000.4 MHz, respectively, corresponding to a ^{13}C Larmor frequency of 125.8 MHz,150.9 MHz, and 251.5 MHz, respectively. Note that in the main text, the ^{1}H Larmor frequency of 1000.4 MHz is referred to as 1 GHz. ^{14}N-^{1}H experiments were performed at a ^{1}H Larmor frequency of 600 MHz and a ^{14}N Larmor frequency of 43.4 MHz. For ^{1}H, ^{13}C and ^{14}N experiments, a 1.3 mm HXY probe at 60 kHz MAS and a 4 mm HXY probe at 12.5 kHz MAS, both in double resonance mode, were utilised. A recycle delay of 16 s (Warwick 500 and 600 MHz), 5 s (Pfizer 500 MHz) or 6 s (1000 MHz) was used. As shown in Figure S7, the ^{1}H T_1 times have been measured to be between 3.1 and 3.4 s (at 60 kHz MAS and a ^{1}H Larmor frequency of 500 MHz by a saturation recovery experiment. Except where otherwise stated, the ^{1}H 90° pulse duration was 2.5 µs and a ^{1}H nutation frequency of 100 kHz was used for homo- and heteronuclear ^{1}H decoupling. In the case of ^{15}N (Pfizer), a 4 mm HFX probe was used at 15 kHz MAS at a ^{15}N Larmor frequency of 50.7 MHz, with a ^{1}H 90° pulse duration of 3 µs. For the ^{19}F spectrum, a 2.5 mm HFX probe at 30 kHz MAS was used at a ^{19}F Larmor frequency of 470.6 MHz for a ^{19}F 90° pulse length of 2.3 µs with ^{1}H decoupling implemented using WALTZ-64.[72] In all 2D experiments, States-TPPI was used to obtain sign-discrimination in F_1.

^{1}H–^{13}C Cross-Polarisation (CP) MAS NMR, ^{1}H–^{15}N CP MAS NMR and ^{1}H–^{13}C CP Heteronuclear Correlation (HETCOR) MAS NMR. CP was achieved using a ramp[73] on ^{1}H, (70-100%) for ^{1}H-^{13}C and (50-100%) for ^{1}H-^{15}N. The nutation frequencies for ^{1}H and ^{13}C during CP were 100 kHz and 62.5 kHz at 500 MHz and 12.5 kHz MAS and 50 kHz and 10 kHz at 1 GHz and 60 kHz MAS.[74,75] The nutation frequencies for ^{1}H and ^{15}N during CP were 79 kHz and 22 kHz at 500 MHz and 15 kHz MAS. SPINAL-64[76] ^{1}H heteronuclear decoupling at 100 kHz (^{1}H-^{13}C, 500 MHz), 10 kHz (^{1}H-^{13}C, 1 GHz),[77] and 84 kHz (^{1}H-^{15}N) was applied during the acquisition of the ^{13}C or ^{15}N FID with a pulse duration of 5.8 µs (^{1}H-^{13}C, 500 MHz), 44.7 µs (^{1}H-^{13}C, 1 GHz), and 5.8 µs (^{1}H-^{15}N). The phase cycling employed was as follows: ^{1}H 90° pulse (90° 270°), CP contact pulse (2{0°} 2{180°} 2{90°} 2{270°}), receiver (0° 180° 180° 0°

90° 270° 270 °90°). For HETCOR at 500 MHz and 12.5 kHz MAS, frequency switched Lee-Goldburg (FSLG)[78] homonuclear ^{1}H decoupling was applied during the t_1 evolution period. 48 transients were co-added for each of 144 t_1 FIDs using a rotor-synchronised t_1 increment of 80 μs, resulting in an experimental time of 30 hours. For HETCOR at 1 GHz and 60 kHz MAS, no homonuclear ^{1}H decoupling was applied in t_1. 96 transients were co-added for each of the 128 t_1 FIDs using a t_1 increment of 50 μs, resulting in an experimental time of 21 hours.

Fast-MAS (60 kHz) Two-Dimensional ^{1}H Experiments. Spectra were acquired for a ^{1}H double quantum (DQ) experiment with one rotor period of BaBa [18,19] recoupling, a ^{1}H single quantum (SQ) NOESY-like Spin Diffusion experiment and a 2D ^{14}N-^{1}H HMQC[25-28] experiment with 8 rotor periods (133.6 μs) of R^3 recoupling[79,80] with x –x phase inversion for every rotor period of the $n = 2$ ($\upsilon_1 = 2\upsilon_R$) rotary resonance recoupling pulses.[81-83] In all cases, a rotor-synchronised t_1 increment of 16.67 μs was used. The DQ spectra were acquired with 32 coadded transients for each of 164 t_1 FIDs, corresponding to an experiment time of 23 hours, at 600 MHz, and with 64 coadded transients for each of the 164 t_1 FIDs, corresponding to an experimental time of 17 hours at 1 GHz. A 16-step phase cycle was implemented, with $\Delta p = \pm 2$ selected during DQ excitation (4 steps) and $\Delta p = -1$ on the z-filter 90° pulse (4 steps), where p is the coherence order. The phase cycling employed was as follows: ^{1}H BaBa pulses (0° 90° 180° 270°), ^{1}H 90° (z-filter) (4 {0°} 4{90°} 4{180°} 4{270°}), receiver (0° 180° 0° 180° 90° 270° 90° 270° 180° 0° 180° 0° 270° 90° 270° 90°). The HMQC experiment was obtained with 72 coadded transients for each of the 64 t_1 FIDs, corresponding to 21 hours experimental time. A 4-step nested phase cycle was used to select changes in the coherence order $\Delta p = \pm 1$ on the first ^{1}H pulse (2 steps) and $\Delta p = \pm 1$ on the last ^{14}N pulse (2 steps).

Referencing. The ^{13}C and ^{1}H chemical shifts were referenced with respect to tetramethylsilane (TMS) using L-alanine at natural abundance as the secondary reference. The CH_3 group of L-alanine is referenced at 1.1 ppm for the ^{1}H methyl resonance and 177.8 ppm for the ^{13}C carboxylate resonance. This corresponds to adamantane at 1.85 ppm for ^{1}H[84] and 38.5 ppm for ^{13}C[85]. The ^{14}N shifts were referenced with respect to saturated NH_4Cl aqueous solution using β-aspartyl-L-alanine at natural abundance, whereby the NH resonance is at –284 ppm at a ^{1}H

Larmor frequency of 600 MHz, corresponding to liquid CH_3NO_2 at 0 ppm.[27,31,86] For equivalence to the chemical shift scale frequently used in protein ^{15}N NMR, where the alternative IUPAC reference (see Appendix 1 of ref [87]) is liquid ammonia at 50 °C, it is necessary to add 379.5 ppm to the given values.[88] The ^{15}N chemical shifts are also referenced to liquid CH_3NO_2 at 0 ppm. For the ^{19}F spectrum, chemical shifts were referenced with respect to 50/50 v/v trifluoracetic acid/ water (relative to CCl_3F[69]). The accuracy of the experimental shifts is within ±0.2, ±0.1 and ±5 for ^{1}H and ^{19}F, ^{13}C and ^{15}N, and ^{14}N, respectively.

2.6 DFT Calculations

Density functional theory (DFT) calculations were conducted using CASTEP[89] version 19.1. For the full crystal, geometry optimisation with fixed unit cell parameters followed by magnetic shielding calculations to determine the NMR parameters were completed. Distances stated in this paper are for the geometry optimised crystal structure. The Perdew Burke Ernzerhof (PBE) exchange correlation functional[90], a plane-wave basis set with ultrasoft pseudopotentials and a plane-wave cut-off energy of 800 eV were implemented. A minimum Monkhorst-Pack grid spacing of 2π x 0.1 $Å^{-1}$ was used. The GIPAW [56,57] method was used to calculate the NMR parameters: calculated isotropic chemical shifts were determined from the calculated chemical shieldings according to $(\partial_{iso}^{calc}) = \sigma_{ref} - \sigma_{calc}$. It is noted that it is common practice to calculate a specific reference shielding for each system (see, e.g., Table S8 of ref. [65]), though average values over a range of compounds are also available.[91] For ^{1}H and ^{13}C, different reference shieldings were used for high- and low ppm chemical shifts:[92] for ^{1}H, 30.5 ppm for > 6.5 ppm and 30.0 ppm for < 6.5 ppm; for ^{13}C, 169.8 ppm for > 51.8 ppm and 175.0 ppm for < 51.8 ppm. For ^{15}N and ^{19}F, a reference shielding of = –160 ppm and 140 ppm, respectively, was used.

3. Results and Discussion

3.1 Single-Crystal X-ray Diffraction of Lorlatinib

The crystal structure of Lorlatinib has been solved at 100 K (see Table 1). (Note that a crystal structure of the HCl salt of Lorlatinib has been reported by Johnson et al., CSD ZOJLIV.) Figure 1 shows the packing of Lorlatinib along the *a* axis. The two distinct molecules in the asymmetric unit cell, i.e., Z' = 2 (see also Figure S1), are coloured in blue and red in Figure 1.

Figure 2 shows, as cyan dotted lines, the intermolecular NH…N and NH…O hydrogen bonds formed by the NH_2 groups with the pyridine nitrogen and the carbonyl oxygen atoms that hold the chains of Lorlatinib molecules together. Notably, one of the four distinct NH_2 hydrogen atoms, $30b^{II}$, is not involved in a hydrogen bonding interaction. This is evident from Figure 2 that zooms in on the hydrogen bonding arrangements; see the circled region in Figure 1, of the NH_2 protons within the asymmetric unit cell of Lorlatinib.

Table 1: Selected Single-Crystal X-ray Diffraction Data for Lorlatinib, CSD 2205098

Chemical Formula	$C_{21}H_{19}F_1N_6O_2$
Formula Weight (g mol^{-1})	406.421
Crystal System	Monoclinic
Space Group	$P2_1$
a (Å)	11.7809
b (Å)	14.3174
c (Å)	11.7976
α (°)	90
β (°)	94.5681
γ (°)	90
Z	4
Z'	2
Temperature (K)	100
R1 [I > 2σ(I)]	0.0279

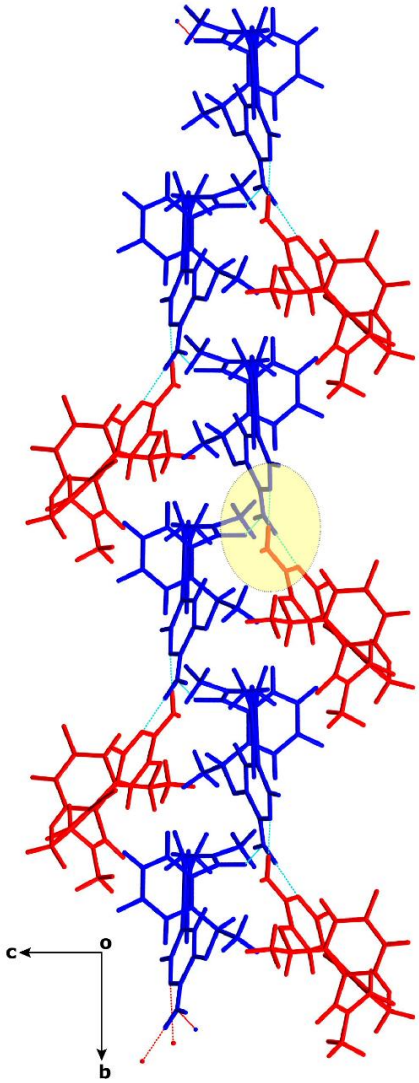

Figure 1: Packing of Lorlatinib along the *a* axis. The blue and red molecules represent molecule I and II in the asymmetric unit cell, respectively. Intermolecular hydrogen bonds are indicated by cyan dotted lines. The circled region encompassing the hydrogen bonding represents the view shown in Figure 2.

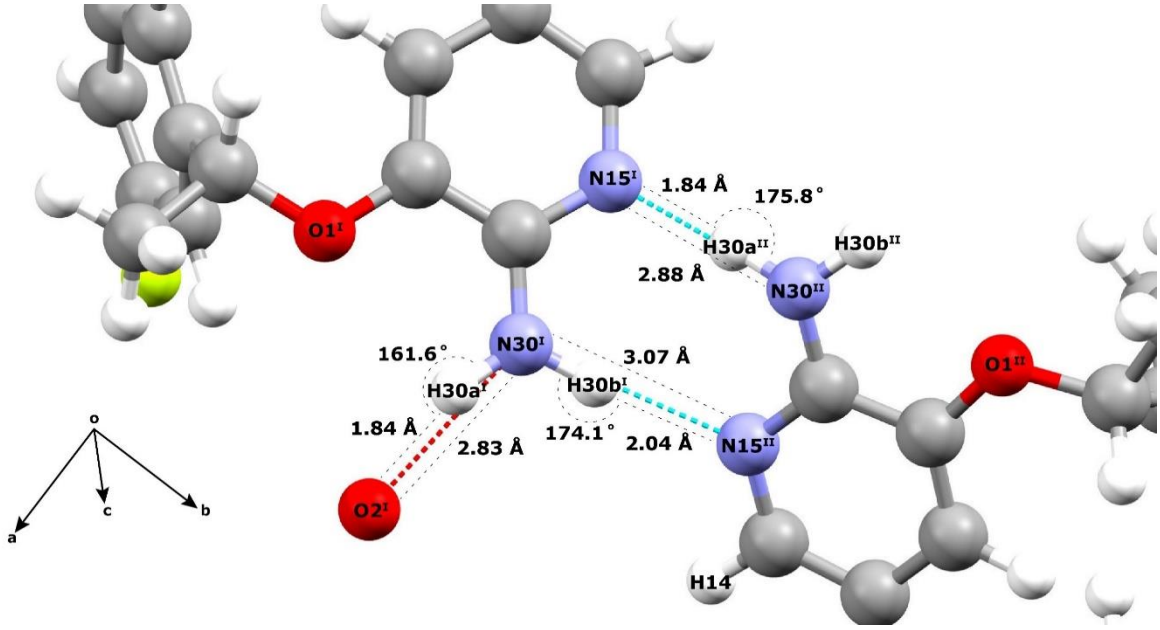

Figure 2: Intermolecular hydrogen bonds exhibited in Lorlatinib by the NH_2 protons as hydrogen bond donors. Note that one of the NH_2 protons, $30b^{II}$, does not have a hydrogen-bonding partner.

3.2 NMR Crystallography of Lorlatinib: Integrating One- and Two-Dimensional MAS NMR Spectroscopy with GIPAW Calculation

In the following sections, we demonstrate how an NMR crystallography analysis that combines solid-state MAS NMR experiment of powdered Lorlatinib with DFT calculation for the crystal structure of Lorlatinib enables, first, assignment of the NMR chemical shifts and, subsequently, insight into intermolecular interactions that affect solubility and bioavailability of a pharmaceutical. For moderately sized organic molecules such as Lorlatinib, key to this strategy is recording two-dimensional correlation MAS NMR spectra.[93]

We show first (in section 3.2.1) how peaks at the ^{13}C and ^{1}H chemical shifts can be selectively observed for directly-bonded CH, CH_2 and CH_3 moieties in two-dimensional ^{1}H-^{13}C heteronuclear correlation solid-state NMR spectra. (Note that the order of nuclei refers to the evolution in the t_1 and t_2 dimensions of the two-dimensional NMR experiment.) A complete assignment of the experimental NMR chemical shifts is achieved for Lorlatinib by comparison to a combination of the known solution-state NMR chemical shifts and NMR chemical shifts calculated using the DFT-based

GIPAW method as applied to periodic crystal structures. When comparing experimental and GIPAW calculated chemical shifts, an extensive literature shows that the discrepancy is usually within 1% of the typical chemical shift range, i.e., ±0.2 and ±2 ppm for ^{1}H and ^{13}C, respectively,[55,94] though some larger deviations have been noted for specific chemical moieties.[95] ^{13}C chemical shifts for non-protonated carbons in Lorlatinib are determined from a one-dimensional ^{1}H-^{13}C CP MAS spectrum. The presence of two distinct molecules in the asymmetric unit cell, i.e., Z' = 2 (see section 3.1) is evident in the doubling of resonances.[96]

As is the case with Lorlatinib, there is often particular interest in hydrogen bonding exhibited by hydrogen atoms that are directly bonded to nitrogen. In this case, nitrogen-hydrogen correlation spectra provide invaluable insight, as shown below in section 3.2.2. Here, it is to be noted that there are two NMR-active nuclei for nitrogen, ^{14}N and ^{15}N, with natural abundances of 99.6% and 0.4%, respectively. Most nitrogen NMR is performed for the low natural abundance ^{15}N nucleus since it has spin I = 1/2 as is the case also for ^{1}H and ^{13}C, and a one-dimensional ^{1}H-^{15}N CP MAS spectrum is also presented for Lorlatinib. The high natural abundance ^{14}N nucleus has spin I = 1 and its NMR spectra are affected by strong quadrupolar interactions between the electric quadrupole moment of the nucleus and the surrounding electric field gradient. Nevertheless, taking advantage of high magnetic field and fast MAS, it is possible to record ^{1}H-detected two-dimensional ^{14}N-^{1}H heteronuclear correlation solid-state NMR spectra as shown in section 3.2.2. The ^{14}N shift of each distinct nitrogen site is the sum of the isotropic chemical shift and the isotropic second-order quadrupolar shift whose magnitude depends on the strength of the quadrupolar interaction (and is also inversely proportional to the B_0 magnetic field). Thus, ^{14}N shifts can show large variations from the peak positions in a ^{1}H-^{15}N CP MAS spectrum that depend only on the isotropic chemical shift. As shown in section 3.2.2 for Lorlatinib, NMR crystallography also allows the prediction via the GIPAW method of both chemical shielding due to the electronic environment of a nucleus and the electric field gradient, and hence the separate isotropic chemical shift and the isotropic second-order quadrupolar shift.

The third valuable two-dimensional NMR experiment for characterising the solid-state structure and packing of moderately sized organic molecules such as the pharmaceutical Lorlatinib is the ^{1}H-^{1}H double-quantum (DQ) single-quantum (SQ) homonuclear correlation experiment, as presented in section 3.2.3. The creation of

DQ coherence between two ^{1}H spins relies on a dipolar coupling between the two spins, with the dipolar coupling having an inverse cubed dependence on the internuclear distance. Thus, with the ^{1}H chemical shifts assigned, the presence or absence of DQ correlation peaks is indicative of the close proximity, typically up to 3.5 Å, or not of two hydrogen atoms.

Taken altogether, this paper presents a complete assignment of the ^{1}H, ^{13}C, $^{14/15}$N and also ^{19}F NMR chemical shifts as well as the ^{14}N quadrupolar parameters for Lorlatinib in the solid state. As noted above, the presence of two distinct molecules in the asymmetric unit cell (see section 3.1) is evident in the doubling of resonances. This work highlights the value of the combination of high magnetic field, here up to a ^{1}H Larmor frequency of 1 GHz, and fast MAS, here up to 60 kHz. As compared to spectra recorded at moderate ^{1}H Larmor frequency (500 MHz), enhanced resolution is particularly evident in the ^{1}H-^{13}C heteronuclear and ^{1}H-^{1}H DQ - SQ homonuclear correlation experimental solid-state MAS NMR spectra.

A concluding discussion (section 4) considers the structural insights that the NMR crystallography analysis offers for Lorlatinib, in particular concerning intermolecular hydrogen bonding that holds the individual molecules together in the solid-state structure, and is thus relevant for the key property for an orally delivered pharmaceutical, namely solubility and hence bioavailability.

3.2.1 Heteronuclear ^{1}H-^{13}C Two-Dimensional MAS NMR Spectra of Lorlatinib: Assigning the ^{13}C and ^{1}H Chemical Shifts

While the near 100% natural abundance and high gyromagnetic ratio of ^{1}H deliver high sensitivity, in the solid-state, resolution is severely affected by line broadening due to strong ^{1}H-^{1}H dipolar couplings – note that this line broadening is absence in solution-state NMR of small and moderately sized molecules due to the rapid molecular tumbling that occurs in solution. In solid-state NMR, there are two strategies for achieving high resolution in the ^{1}H dimension. First, increasing the MAS frequency narrows the ^{1}H resonances. Alternatively, a moderate MAS frequency can be combined with ^{1}H homonuclear decoupling.

Figure 3 presents two-dimensional ^{1}H-^{13}C heteronuclear correlation (HETCOR) MAS NMR spectra of Lorlatinib, recorded using the two alternative strategies for achieving high resolution in the ^{1}H dimension. The spectra in the bottom row, Figure

3c and 3d, were recorded at a MAS frequency of 60 kHz with no ^{1}H homonuclear decoupling applied. Separate spectra were recorded for the aromatic (left, c) and aliphatic (right, d) ^{13}C resonances. In the top row, two zoomed-in regions corresponding to the same aromatic (left, a) and aliphatic (right, b) ^{13}C resonances are shown, as extracted from a ^{1}H-^{13}C HETCOR MAS NMR spectrum recorded at a MAS frequency of 12.5 kHz, applying frequency-switched Lee-Goldburg (FSLG)[78] ^{1}H homonuclear decoupling during the evolution of ^{1}H transverse magnetisation in the indirect (t_1) dimension. A drawback of applying ^{1}H homonuclear decoupling is that the range of ^{1}H chemical shifts is reduced by a scaling factor that depends on how the rf pulses that achieve the ^{1}H homonuclear decoupling are implemented experimentally. The spectra presented in Figure 3a and 3b have been processed such that the highest and lowest ^{1}H chemical shifts in ppm are the same as those with MAS alone in Figure 3c and 3d. A further difference is that the spectra are recorded at a ^{1}H Larmor frequency of 500 MHz (top row, Figure 3a and 3b) or 1 GHz (bottom row, Figure 3c and 3d). High magnetic field brings the benefit of both higher sensitivity and enhanced resolution, the latter provided that the linewidths are independent of magnetic field. In both cases, CP was employed to transfer magnetisation from ^{1}H to ^{13}C via ^{1}H-^{13}C heteronuclear dipolar couplings. Note that at 60 kHz MAS, a low ^{13}C nutation frequency of 10 kHz was applied during CP such that the presented spectra had to be separately recorded for the high-ppm (aromatic) and low-ppm (aliphatic) regions, as presented in Figure 3c and 3d, respectively.

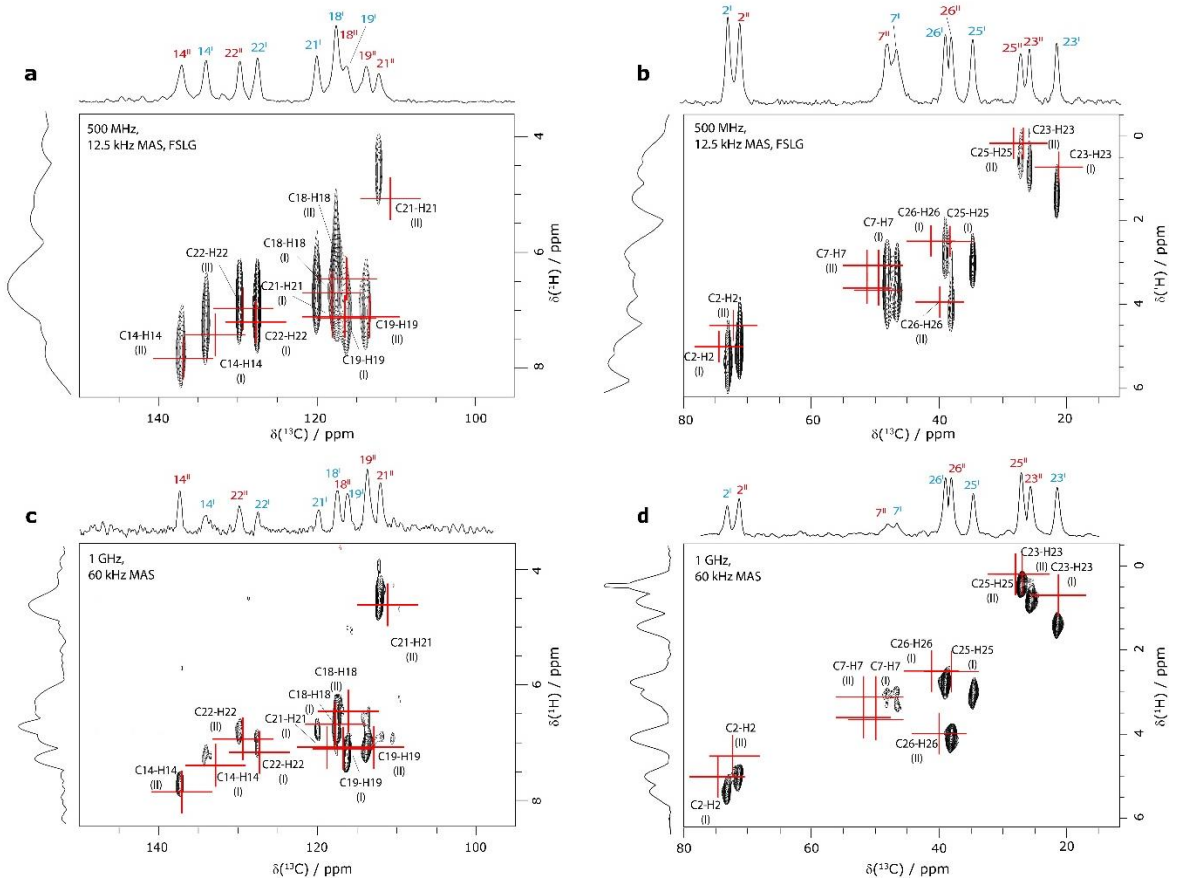

Figure 3: ^{1}H-^{13}C CP-HETCOR two-dimensional MAS (12.5 kHz) NMR spectra with skyline projections of Lorlatinib recorded at a ^{1}H Larmor frequency of (a, b) 500 MHz or (c, d) 1 GHz and a MAS frequency of (a, b) 12.5 kHz of (c, d) 60 kHz and a CP contact time of (a, b) 250 µs or (c, d) 500 µs. For (a, b), ^{1}H FSLG homonuclear decoupling was applied in t_1. Separate zoomed-in regions are shown for the (a, c) aromatic and (b, d) aliphatic ^{13}C regions. Calculated GIPAW chemical shifts are shown as red crosses for directly bonded CH connectivities up to 1.1 Å. The base contour level is at 18%, 25% and 14% of the maximum peak height for (a and b), (c) and (d), respectively.

For the relatively short CP contact times, 250 µs for Figures 3a and 3b or 500 µs in Figures 3c and 3d, the observed cross peaks are predominantly characteristic of one-bond C-H connectivities. The spreading out of resonances into a second dimension is particularly valuable for the crowded aromatic region, where eight distinct CH peaks are observed between 6.7 and 7.7 ppm in Figures 3a and 3c, for ^{13}C chemical shifts between 116.3 and 137.1 ppm. For each of the protonated carbon atoms, with the exception of C18, distinct peaks are observed in the two-dimensional

^{1}H-^{13}C spectra corresponding to the two distinct molecules in the asymmetric unit cell, *Z*' = 2 (labelled as I and II). For the C25 methyl resonances, there is a large difference for the ^{1}H chemical shifts in the two distinct molecules, namely 3.0 and 0.5 ppm. This is discussed further in section 4 below.

Red crosses in Figure 3 correspond to the GIPAW calculated ^{1}H and ^{13}C chemical shifts for the DFT (CASTEP) geometry-optimised crystal structure. The assigned ^{13}C and ^{1}H resonances as labelled in Figure 3 are listed in Table 2. Good agreement is observed between the experimental and GIPAW calculated chemical shifts, with most within the usual 1% of the typical chemical shift range, i.e., ±0.2 and ±2 ppm for ^{1}H and ^{13}C, respectively.[55,94] DFT is not perfect and, as observed in the literature for other systems, there are some larger discrepancies, notably, for ^{1}H, at the low-ppm end, i.e., a discrepancy of 0.6 and 0.7 ppm for the C23 methyl protons. This may be explained by the often observed phenomenon that a plot of calculated NMR shielding against experimental chemical shift usually shows a small deviation from minus one,[55,96,97] i.e., for low-ppm resonances, GIPAW calculated ^{1}H chemical shifts are then lower than those observed experimentally, as is the case for the C23 methyl protons.

Table 2 also lists solution-state ^{13}C and ^{1}H as measured in DMSO. The differences between experimental solution- and solid-state NMR ^{13}C chemical shifts are also observed to be mostly within ±2 ppm. Greater variation is observed for the ^{1}H chemical shifts, noting the greater sensitivity of the ^{1}H chemical shift to the solid-state packing, e.g., ring currents from the aromatic groups (as discussed in section 4 below, see also the discussion of the NH_2 ^{1}H chemical shifts in section 3.2.3 below).

Table 2: Experimental solution- (DMSO) and solid-state and GIPAW calculated ^{1}H and ^{13}C NMR chemical shifts (in ppm) for Lorlatinib

	Solution-State		**Solid-State[a]**		**GIPAW Calculated**	
Atom No.	^{1}H	^{13}C	^{1}H	^{13}C	^{1}H	^{13}C
2	5.6	70.7	5.4^{I}, 5.1^{II}	71.2^{II}, 73.0^{I}	5.0^{I}, 4.5^{II}	72.4^{II}, 74.3^{I}
3	-	143.4	-	142.0	-	143.4^{II}, 144.3^{I}

4[b]	-	132.6	-	125.4[I] / 131.6[I], 131.9[II]	-	130.5[I], 132.1[II]
5[c]	-	167.7	-	162.7[II] / 163.7[II] 167.9[I] / 170.2[I]	-	166.5[II], 169.4[I]
7a	4.2	46.4	3.6[I], 3.6[II]	46.6[I], 48.1[II]	3.1[I], 3.6[II]	49.9[I], 51.9[II]
7b	4.4		3.4[I], 3.4[II]		3.7[I], 3.1[II]	
8	-	143.7	-	143.7[I], 144.7[II]	-	140.5[I], 144.5[II]
11	-	111.2	-	112.2	-	110.2[I], 110.9[II]
12[b]	-	127.1	-	125.4[I] / 131.6[I], 131.9[II]	-	130.2[I], 133.2[II]
13	-	112.6	-	116.3	-	113.1[I], 114.5[II]
14	7.6	136.6	7.3[I], 7.7[II]	134.0[I], 137.1[II]	7.4[I], 7.8[II]	133.1[I], 137.1[II]
16	-	150.9	-	150.8[I], 151.7[II]	-	147.1[I], 149.3[II]
17	-	138.1	-	139.4[II], 139.7[I]	-	139.4[II], 140.5[I]
18	6.8	118.5	6.7[I], 6.7[II]	117.5[I] 117.5[II]	6.7[I], 6.4[II]	115.9[II], 118.3[I]
19	7.6	113.7	7.2[I], 7.1[II]	113.8[II], 116.3[I]	7.2[I], 7.1[II]	113.2[II], 117.0[I]
20[c]	-	162.8	-	167.9[I] / 170.2[I], 162.7[II] / 163.7[II]	-	168.8[II], 169.7[I]

21	7.2	115.0	6.8^{I}, 4.6^{II}	112.2^{II} 119.8^{I}	7.1^{I}, 4.6^{II}	111.3^{II}, 118.3^{I}
22	7.5	128.5	7.0^{I}, 6.9^{II}	127.4^{I} 129.7^{II}	7.3^{I}, 6.9^{II}	127.7^{I}, 129.3^{II}
23[d]	1.7	21.9	1.4^{I}, 0.8^{II}	21.5^{I}, 25.8^{II}	0.7^{I}, 0.2^{II}	21.4^{I}, 27.0^{II}
25[d]	3.0	30.9	3.0^{I}, 0.5^{II}	27.2^{II}, 34.7^{I}	2.5^{I}, 0.2^{II}	28.1^{II}, 37.8^{I}
26[d]	4.0	38.6	2.8^{I}, 4.1^{II}	38.0^{II}, 39.0^{I}	2.5^{I}, 3.9^{II}	39.9^{II}, 41.4^{I}
27	-	111.0	-	113.9	-	116.5^{I}, 117.0^{II}
30a	6.2	-	7.0^{I}, 7.0^{II}	-	8.8^{I}, 10.3^{II}	-
30b		-	7.0^{I}, 4.0^{II}	-	9.5^{I}, 4.0^{II}	-

[a] See MAS NMR spectra in Figures 3, 4, 6, 7 and 8. [b] In this case, there is ambiguity in the experimental assignments of the atoms 4 and 12. [c] In this case, there is ambiguity in the experimental assignments of the atoms 5 and 20. [d] For CH_3 groups, the average over the three GIPAW calculated ^{1}H chemical shifts is given.

Figure 4a presents a one-dimensional ^{1}H (500 MHz)-^{13}C CP MAS (12.5 kHz) NMR spectrum of Lorlatinib that was recorded with a CP contact time of 1.25 ms. Asterisks in Figure 4a denote spinning sidebands that are observed at 99 ppm (corresponding to 12.5 kHz at the ^{13}C Larmor frequency of 125.8 MHz) away from the centreband for carbonyl, aromatic and alkyne ^{13}C resonances that exhibit large chemical shift anisotropies. Note that in a CP MAS spectrum, the peak intensity depends on the transfer of transverse magnetisation from ^{1}H to ^{13}C during the CP contact time. The build-up of CP signal as a function of the contact time depends on the ^{1}H-^{13}C dipolar couplings that also determine the loss of signal due to $T1\rho$ relaxation during the ^{1}H spin-lock pulse: hence different build-up behaviour is observed for quaternary and non-quaternary ^{13}C resonances, and also between CH, CH_2 and CH_3 resonances. Therefore, CP MAS spectra are not quantitative. Nevertheless, similar, but not identical, peak intensities are observed for similar chemical environments, notably for ^{13}C resonances corresponding to the same chemical shift in the two distinct molecules in the asymmetric unit cell. Figure S5 presents integrated intensities for the resolved centre-band resonances.

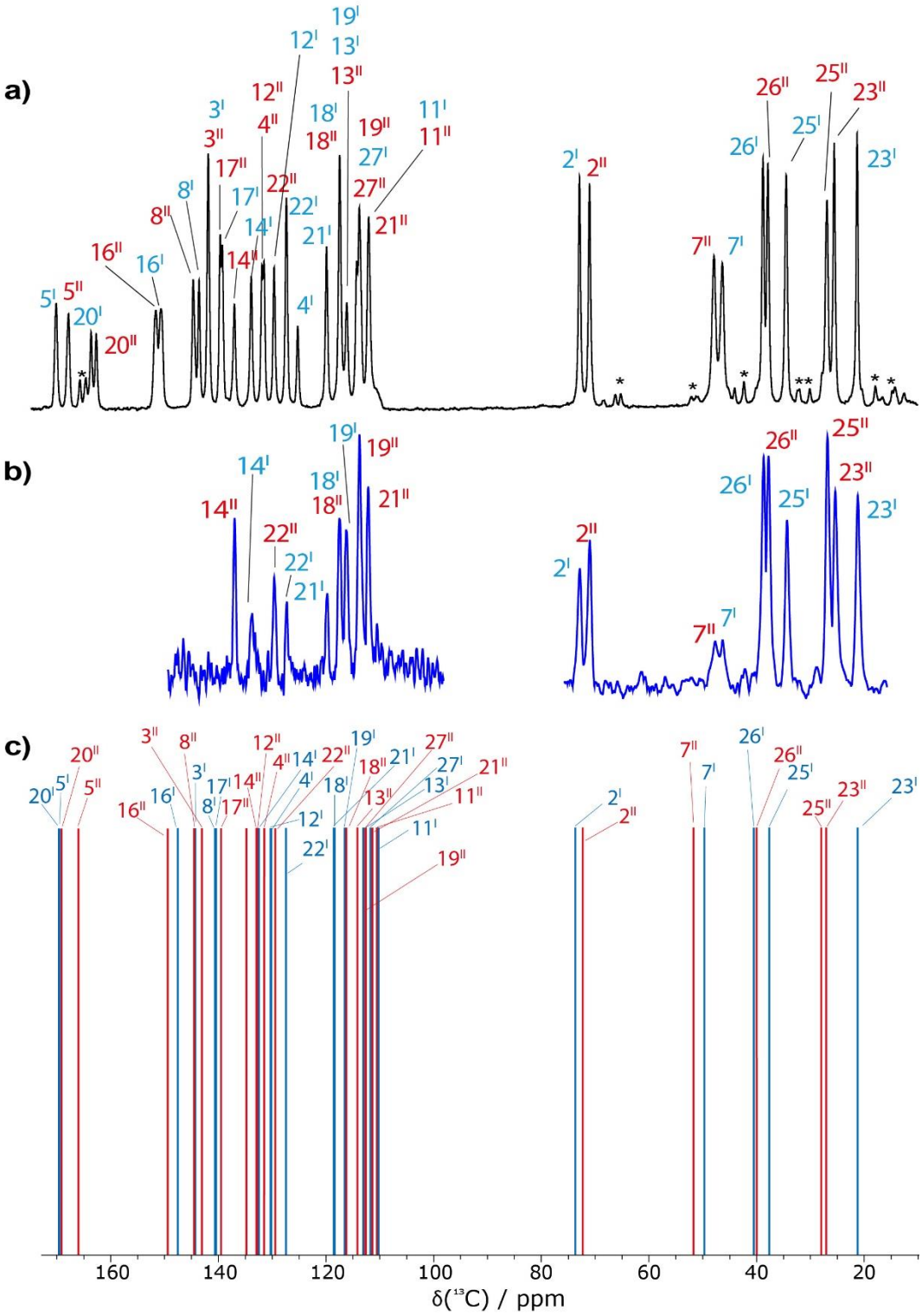

Figure 4: (a) A 1D ^{1}H (500 MHz) – ^{13}C CP (1.25 ms) MAS (12.5 kHz) NMR spectrum of Lorlatinib acquired with 4,096 co-added transients. Asterisks denote spinning sidebands. (b) Skyline projections from the ^{1}H (1 GHz) -^{13}C HETCOR MAS (60 kHz) CP (500 μs) -HETCOR NMR spectra presented in Figure 3c and 3d. (c) The stick spectrum represents the GIPAW calculated ^{13}C chemical shifts for the two distinct molecules (blue^{I} and red^{II}) in the asymmetric unit cell (see also Table 2).

In Figure 4, the CP MAS spectrum in Figure 4a is compared to Figure 4b that presents skyline projections from the ^{1}H (1 GHz) -^{13}C HETCOR MAS (60 kHz) CP-HETCOR NMR spectra presented in Figure 3c and 3d that were recorded with a shorter CP contact time of 500 μs. Additional ^{13}C resonances are observed in Figure 4a for the non-protonated quaternary carbon atoms. In addition, Figure 4c presents stick spectra that correspond to the GIPAW calculated chemical shifts. Note that the blue (I) and red (II) colouring for the stick spectra corresponding to the two distinct Lorlatinib molecules in the asymmetric unit cell. The non-protonated ^{13}C resonances are assigned in the same order as the GIPAW calculated values, though, as noted in Table 2, there is ambiguity concerning the assignment of the C4 and C12 and the C5 and C20 pairs of resonances.

3.2.2 Heteronuclear ^{1}H-^{15}N and ^{14}N-^{1}H MAS NMR Spectra of Lorlatinib: $^{14/15}$N Chemical Shifts and ^{14}N Quadrupolar Parameters

A ^{1}H-^{15}N CP MAS NMR spectrum of Lorlatinib is presented in Figure 5. Even though, compared to ^{13}C, ^{15}N has a lower natural abundance (0.4% compared to 1.1%) and a lower magnetogyric ratio and hence Larmor frequency (51 MHz compared to 126 MHz), the spectrum could be recorded for spin I = 1/2 ^{15}N nucleus in an experimental time of 28 hours, compared to 18 hours for the ^{1}H-^{13}C CP MAS NMR spectrum in Figure 4. As discussed above, such a CP MAS spectrum is not quantitative, though similar intensity is observed for the ^{15}N resonances corresponding to the two distinct molecules in the asymmetric unit cell, where differences are resolved for N6, N10, N28 and N30. Figure S6 presents integrated intensities for the resolved resonances. The GIPAW calculated ^{15}N chemical shifts are represented in Figure 5 as a stick spectrum, with blue and red lines distinguishing molecule I and II. Table S1 compares the experimental and GIPAW-calculated ^{15}N chemical shifts. The GIPAW calculation reproduces the experimental observation of a single superimposed peak for the two distinct molecules for N15 and N9 (for N9, there is a hint that two resonances are present in the experimental spectrum).

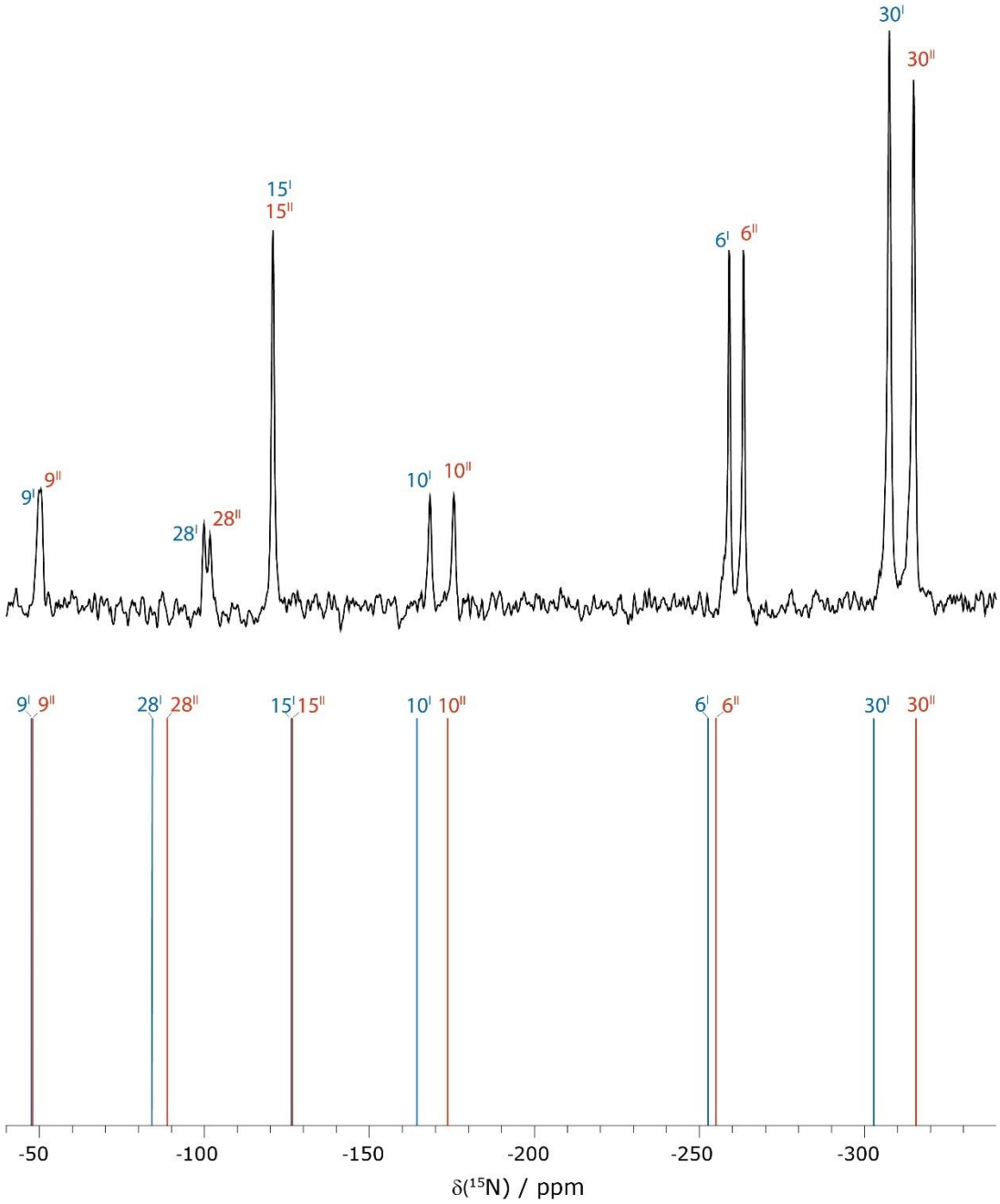

Figure 5: (Top) A 1D ^{1}H (500 MHz) – ^{15}N CP (3.5 ms) MAS (15 kHz) NMR spectrum of Lorlatinib acquired with 20,480 co-added transients. (Bottom) The stick spectrum represents the GIPAW calculated ^{15}N chemical shifts (see also Table 3) for the two distinct molecules (blue^{I} and red^{II}) in the asymmetric unit cell.

Alongside ^{1}H-^{13}C heteronuclear and ^{1}H-^{1}H DQ-SQ homonuclear correlation spectra that are discussed in the previous and next section, respectively, a third valuable two-dimensional MAS NMR correlation experiment that can be applied to small and moderately sized organic molecules such as pharmaceuticals is a ^{14}N-^{1}H heteronuclear multiple-quantum coherence (HMQC) MAS NMR experiment. Such an

experiment utilises the 99.6% natural abundance, but spin $I = 1$, ^{14}N nucleus.[26-28,98] It is informative to view the three ^{1}H-based two-dimensional spectra in a column view with a common (horizontal) ^{1}H axis. Such a view is presented for Lorlatinib in Figure 6, with a ^{1}H-^{1}H DQ-SQ MAS NMR spectrum at the top (Figure 6a), a ^{14}N-^{1}H HMQC MAS NMR spectrum in the middle (Figure 6b) and a ^{1}H-^{13}C CP-HETCOR spectrum at the bottom (Figure 6c). The latter corresponds to the same spectrum as was presented in Figures 3a and 3b, but the view is rotated through 90 degrees so that the three spectra have the same horizontal ^{1}H axis (note that this then means that the ^{13}C axis unusually runs from high to low ppm on moving down the page). Dashed vertical lines identify the ^{1}H chemical shifts for the different hydrogen atoms in the two distinct molecules in the asymmetric unit cell. These are labelled in the skyline projection at the top of the figure, noting the blue and red colours for molecules I and II.

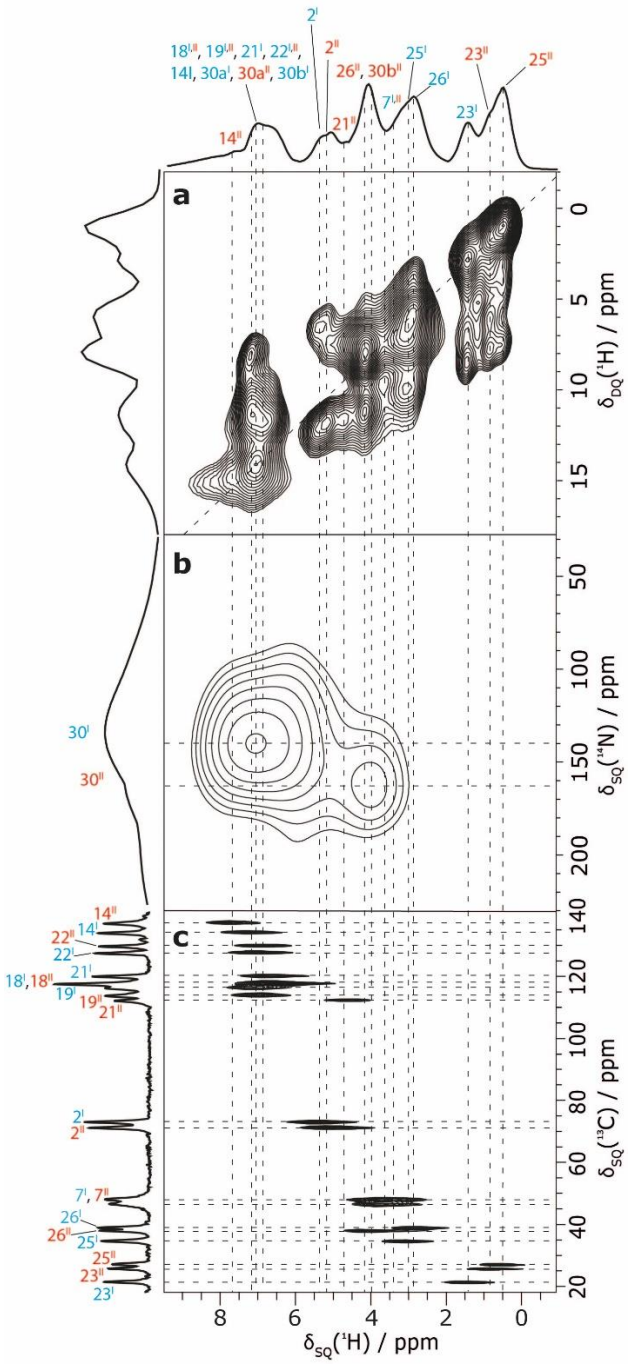

Figure 6: 2D MAS (60 kHz) NMR spectra with skyline projections of Lorlatinib: (a) a ^{1}H (600 MHz) -^{1}H DQ-SQ spectrum recorded with one rotor period of BaBa recoupling; (b) a ^{14}N-^{1}H (600 MHz) HMQC spectrum recorded with 8 rotor periods of R^3 recoupling (recoupling time = 133.6 μs); (c) a ^{1}H (500 MHz) —^{13}C CP (250 μs)-HETCOR MAS (12.5 kHz) two-dimensional NMR spectrum corresponding to directly bonded CH connectivities up to 1.1 Å (as presented in Figures 3a and 3b, but rotated clockwise through 90º such that the ^{13}C axis is from high to low ppm downwards).

The base contour levels are at (a) 9%, (b) 51% and (c) 18% of the maximum peak height, respectively.

In this section, we focus on the ^{14}N-^{1}H HMQC MAS NMR spectrum of Lorlatinib presented in Figure 6b that was recorded at a ^{1}H Larmor frequency of 600 MHz and a MAS frequency of 60 kHz. Here, heteronuclear correlation is established by the recoupling of the ^{14}N-^{1}H dipolar couplings that are otherwise removed by MAS. Specifically, phase-inverted rotary-resonance recoupling (R^3) was employed[79-83] with the ^{1}H nutation frequency set equal to twice the MAS frequency, i.e., to 120 kHz. A short recoupling time of 133.6 μs was used such that predominantly only one-bond N-H connectivities are probed, i.e. for the N30 NH_2 groups. Two distinct peaks are resolved in Figure 6b, corresponding to two distinct ^{14}N shifts of 139 and 162 ppm and two distinct ^{1}H chemical shifts of 7.0 and 4.0 ppm. Figure 6 thus shows that some of the NH_2 ^{1}H resonances overlap with the already crowded aromatic region at 7 ppm. The low-ppm NH_2 ^{1}H resonance at 4.0 ppm overlaps with one of the N-Me CH_3 ^{1}H resonance at 4.1 ppm.

It is evident that the two ^{14}N shifts of 139 and 162 ppm in Figure 6b are very different to the two ^{15}N isotropic chemical shifts of −307.5 and −316.0 ppm in Figure 5. This is because, since ^{14}N is a spin I = 1 nucleus, ^{14}N solid-state NMR spectra are affected by the quadrupolar interaction between the electric quadrupole moment of the ^{14}N nucleus and the surrounding electric field gradient. The ^{14}N quadrupolar interaction is typically on the order of MHz and is thus of comparable size to the ^{14}N Larmor frequency, 43.4 MHz for the spectrum presented in Figure 6b. This is different to the case of dipolar couplings and chemical shift anisotropy that are of the order of kHz. As such, second-order perturbation theory must be applied in order to explain observed ^{14}N solid-state NMR spectra. There are two key manifestations of this: first, fourth-rank second-order quadrupolar broadening of the ^{14}N lineshapes that is not removed by MAS (contrast this with second-rank broadening due to dipolar couplings and chemical shift anisotropy and also first-order quadrupolar broadening that are all removed by MAS); second, an isotropic second-order quadrupolar shift[27] that is additional to the isotropic chemical shift, the latter is assumed to be the same for ^{15}N and ^{14}N. As shown in Table 3, the isotropic second-order quadrupolar shifts are large,

namely 454 and 470 ppm, hence explaining the substantial changes in the ^{14}N shifts as compared to the ^{15}N isotropic chemical shifts.

Table 3: A comparison of the experimentally determined and GIPAW calculated ^{14}N and ^{15}N chemical shifts for Lorlatinib.

Site	$\delta(^{15}N)_{exp}$[a] (ppm)	$\delta(^{15}N)_{calc}$[b] (ppm)	$\delta(^{14}N)_{exp}$[c] (ppm)	$\delta^{Q}iso(^{14}N)_{exp}$[d] (ppm)	P_{Qexp}[e] (MHz)	P_{Qcalc} (MHz)
30[I]	−314.9	−316.0	139	454	3.4	−3.6
30[II]	−307.5	−303.1	162	470	3.4	−3.3

a ^{15}N isotropic chemical shift values as taken from the ^{1}H-^{15}N CP MAS spectrum presented in Figure 5.

b $\delta_{iso} = \sigma_{ref} - \sigma_{iso}$, where $\sigma_{ref} = -160$ ppm

c Centre of gravity of the ^{14}N peaks extracted from the ^{14}N-^{1}H HMQC spectrum seen in Figure 6b. Here, the error is estimated to be within ±5 ppm

d $\delta^{Q}iso(^{14}N)_{exp} = \delta(^{14}N)_{exp} - \delta(^{15}N)_{expt}$

e P_{Qexp} is calculated from $\delta^{Q}iso(^{14}N)_{exp}$ using the equation: [27]

$\delta_{iso}^{Q} = (3/40)\,(P_Q/\nu_0)^2 \times 10^6$, where $P_Q = C_Q\sqrt{\left[1 + (n_Q^2/3)\right]}$. Note that the sign of P_Q cannot be determined from an experimental ^{14}N-^{1}H HMQC MAS NMR spectrum.

By means of the two-dimensional ^{14}N-^{1}H HMQC MAS NMR spectrum presented in this section (Figure 6b) and the two-dimensional ^{1}H-^{13}C CP-HETCOR MAS NMR spectra presented in Figure 6c and in the previous section (Figure 3), together with the GIPAW calculation, a full assignment of the ^{1}H chemical shifts is achieved (see Table 2). Figure 7 compares one-pulse ^{1}H MAS NMR spectra of Lorlatinib obtained at a ^{1}H Larmor frequency of 600 MHz (black) or 1 GHz (purple). Enhanced resolution is obtained at 1 GHz, allowing the resolution of new peaks, though the complete assignment relies on the two-dimensional spectra presented in Figure 6.

Figure 7 also allows a comparison to the GIPAW calculated ^{1}H chemical shift that are represented in the stick spectrum at the bottom. As was evident from the ^{1}H-^{13}C CP-HETCOR MAS NMR spectra presented in Figure 3, where red crosses correspond to the GIPAW calculated chemical shifts, there is good agreement between experiment and calculation for the ^{1}H resonances between 2 and 8 ppm, i.e., nearly all are within 0.2 ppm corresponding to the usual 1% of the ^{1}H chemical shift range. The discrepancies for the C23 methyl ^{1}H resonances in the low-ppm region have been discussed in section 3.2.1.

It is evident from Figure 7 that the GIPAW calculated ^{1}H chemical shifts for the high-ppm NH_2 resonances, namely 30a^{I}, 30b^{I}, and 30a^{II} at 8.8, 9.5 and 10.3 ppm are significantly higher than the experimental value of 7.0 ppm. Such a discrepancy is well established for hydrogen-bonded ^{1}H resonances and can be explained by the known experimental temperature-dependence of such hydrogen-bonded ^{1}H chemical shifts[99-107], whereas GIPAW calculation is effectively performed at 0 K.[108] In other words, if variable-temperature ^{1}H MAS NMR spectra were recorded, these ^{1}H resonances would move to higher ppm as the temperature is lowered.

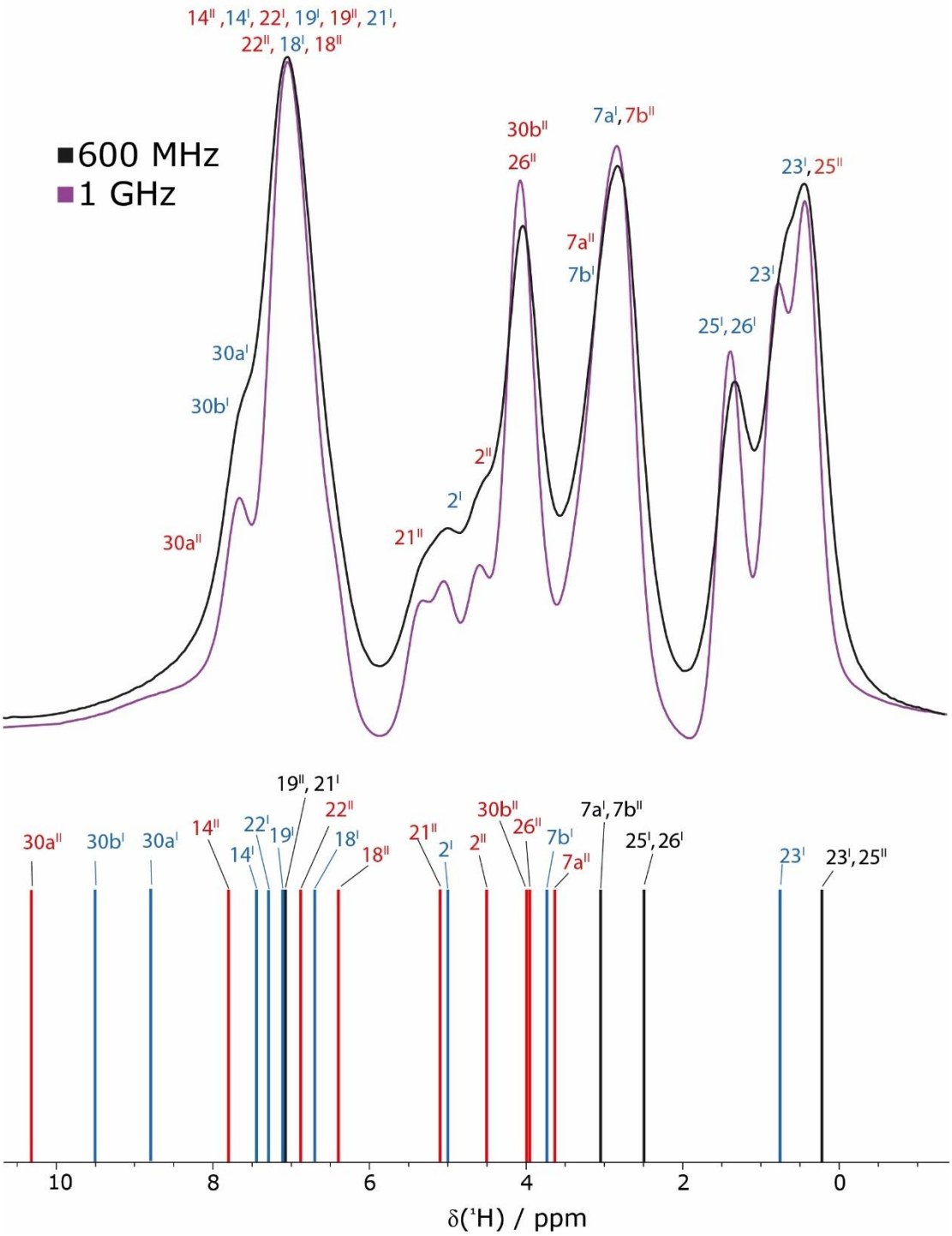

Figure 7: (Top) One-pulse ^{1}H MAS (60 kHz) NMR spectra of Lorlatinib obtained at a ^{1}H Larmor frequency of 600 MHz (black) or 1 GHz (purple). 8 transients were co-added. (Bottom) A stick spectrum representing the GIPAW calculated chemical shifts (See also Table 2); blue and red colour coding denote chemical shifts for the two distinct molecules in the asymmetric unit cell, with black colour used where the GIPAW calculated chemical shifts overlap.

3.2.3 H-H proximities in Lorlatinib: ^{1}H (DQ) –^{1}H (SQ) 2D MAS NMR

A ^{1}H-^{1}H DQ-SQ MAS NMR experiment, as shown in Figure 6a, recorded with one rotor period of BaBa recoupling,[18,19] provides information on proximities between protons that are close together in space.[16,93] This spectrum is repeated in Figure 8, which compares the ^{1}H-^{1}H DQ-SQ spectra acquired at 600 MHz and 1 GHz, both at 60 kHz MAS. Here, a clear improvement in the resolution can be noted at the higher magnetic field. It is only possible to create DQ coherence if there is a sufficiently large dipolar coupling, due to a H-H close proximity, noting the inverse cubed dependence on the internuclear distance. The presence of a cross peak at a specific DQ frequency shows that the two protons are in close proximity, usually within 3.5 Å of each other.

Table 4 lists the H..H proximities (<3.5 Å) for all protons in the DFT geometry-optimised structure of Lorlatinib for which a DQ peak is observed in the ^{1}H-^{1}H DQ-SQ MAS NMR spectra presented in Figure 6a and 8. A table of H..H proximities (<3.5 Å) and corresponding DQ frequency, sorted by the numerical proton identifier can be found in the supplementary information (Table S2). As indicated by the vertical dashed lines in Figure 6a and 8, the spreading out into a second dimension in the ^{1}H-^{1}H DQ-SQ spectrum allows the distinction of ^{1}H resonances that overlap in the one-dimensional spectrum.

Consider the ^{1}H SQ resonances below 2 ppm that correspond to the methyl resonances, 23^{I}, 23^{II} and 25^{I}, as assigned by the ^{1}H-^{13}C HETCOR MAS NMR spectra presented in Figure 3 with the GIPAW calculated chemical shifts. As noted in Figure 3, the 23^{II} and 25^{I} resonances are resolved at 1 GHz (see the inset in Figure 8b), allowing the clear identification of the three CH_3 auto peaks on the $F_1 = 2\ F_2$ diagonal (shown as a dashed line). In addition, cross peaks between these methyl protons and the CH (2) and aromatic CH (19 and 22) are observed, as indicated by horizontal solid black bars well as dashed lines in Figure 8. Between 2.5 and 3.5 ppm in the ^{1}H SQ dimension, there are the 25^{I} and 26^{I} CH_3 and the 7a^{I,II} and 7b^{I,II} CH_2 resonances, for which intense auto peaks are observed on the $F_1 = 2\ F_2$ diagonal, as well as a cross peak at δ_{DQ} ~10 ppm corresponding to proximities to aromatic and NH_2 protons. At δ_{DQ} ~4 ppm, there are the 26^{II} CH_3 and the 30b^{II} NH_2 hydrogen atom that does not exhibit intermolecular hydrogen bonding: as well as the CH_3 auto peak on the diagonal, a cross peak at δ_{DQ} ~11.5 ppm is observed corresponding to intra NH_2 proximity to the

higher-ppm $30b^{I}$ NH_2 as well as a proximity of 26^{II} CH_3 hydrogens to the aromatic 19^{II} hydrogen.

The lowest ^1H chemical shift for an aromatic CH is 21^{II} at 4.6 ppm, for which a DQ cross peak at δ_{DQ} = 4.6 + 6.9 = 11.5 ppm corresponding to an intramolecular proximity to the neighbouring 22^{II} hydrogen is observed. The 2^{II} and 2^{I} CH resonances at 5.1 and 5.4 ppm exhibit DQ cross peaks at δ_{DQ} = 5.1 + 6.7 = 11.8 ppm and δ_{DQ} = 5.4 + 6.7 = 12.1 ppm corresponding to an intramolecular proximity to the neighbouring 22^{II} or 22^{I} hydrogen, as well as DQ cross peaks with the CH_3 groups, as discussed above. The crowded region around δ_{SQ} ~ 7 ppm corresponds to three of the NH_2 hydrogens and multiple CH aromatic peaks. In addition to the cross peaks to lower ppm resonances discussed above, an auto peak is observed at δ_{DQ} = 14.2 ppm corresponding to the $30a^{I}$, $30a^{II}$ NH_2 auto peak as well as the 21^{I}-22^{I} intermolecular proximity between the two neighbouring aromatic protons. The highest ^1H chemical shift for an aromatic CH is 14^{I} at 7.7 ppm, for which a cross peak at δ_{DQ} = 7.7 + 7.1 = 14.8 ppm is observed corresponding to an intermolecular proximity to a $30a^{I}$ NH_2 hydrogen.

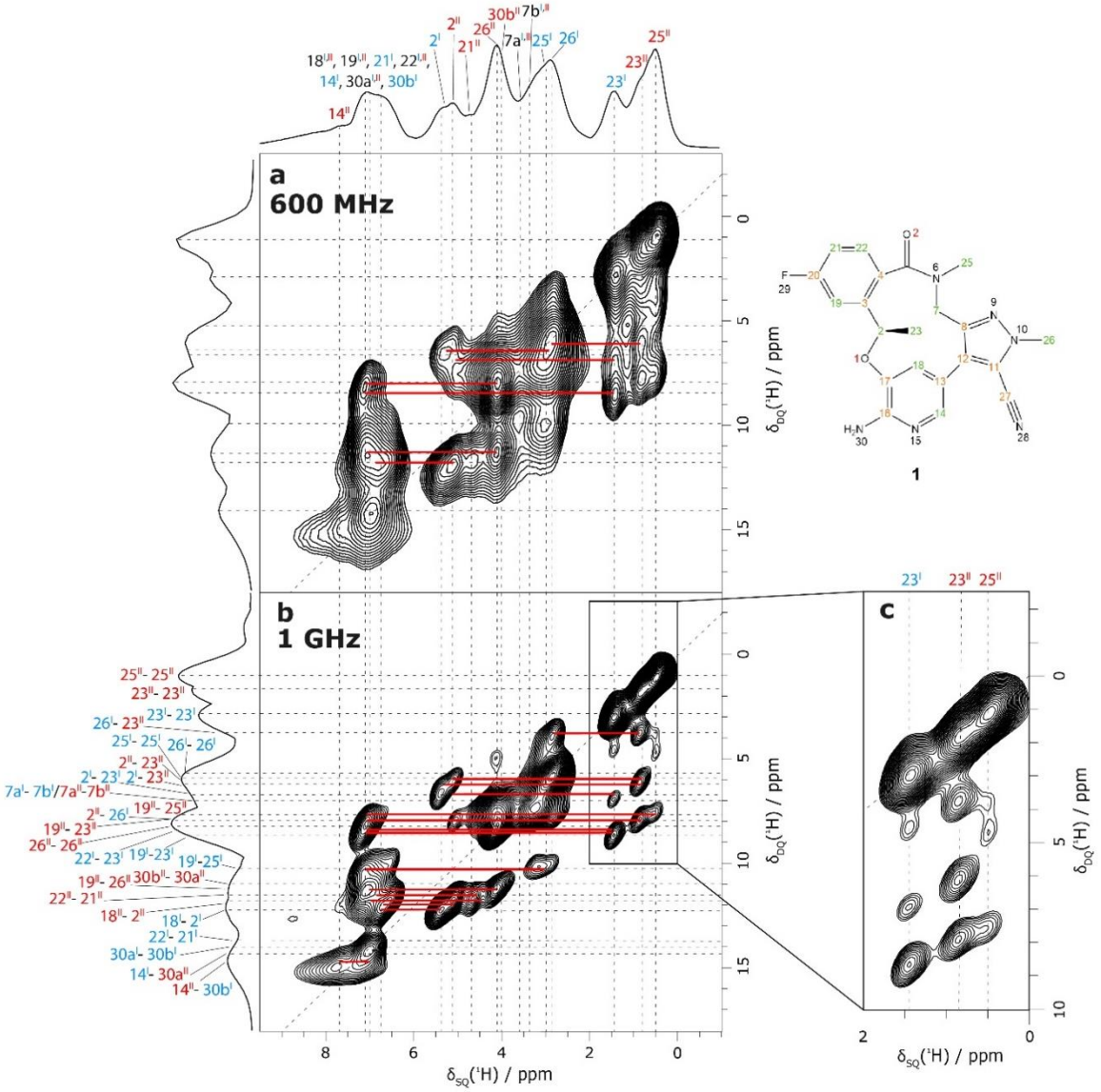

Figure 8: ^{1}H (600 MHz) (a) and ^{1}H (1 GHz) (b) DQ MAS (60 kHz) NMR spectra with skyline projections of Lorlatinib recorded with one rotor period of BaBa recoupling; top is repeated from Figure 6a. (c) A zoomed inset is shown alongside the 1 GHz spectrum for 0 – 2 ppm in the SQ spectrum. The horizontal dashed and thick lines identify DQ peaks at the sum of the two SQ frequencies (see also Table 4). The F_1 = 2 F_2 diagonal is indicated by a dashed line. The base contour levels are at (a) 9% and (b) 8% of the maximum peak height, respectively.

Table 4: H-H proximities (<3.5 Å) corresponding to experimentally observed ^{1}H DQ frequencies (see Figure 6a and 8) as extracted from the DFT geometry-optimised (CASTEP) crystal structure of Lorlatinib.

Proton 1	δ_{SQ1} (ppm)	Proton 2	δ_{SQ2} (ppm)	δ_{DQ} (ppm)	Separation (Å) [a]
25 II (CH_3)	0.5	**25 II (CH_3)**	0.5	1.0	1.78, 1.79, 1.79
23 II (CH_3)	0.8	**23 II (CH_3)**	0.8	1.6	1.77, 1.78, 1.79
23 I (CH_3)	1.4	**23 I (CH_3)**	1.4	2.8	1.77, 1.78, 1.80
26 I (CH_3)	2.8	**23 II (CH_3)**	0.8	3.6	*2.27, 2.57, 2.84, 3.15*
26 I (CH_3)	2.8	**26 I (CH_3)**	2.8	5.6	1.78, 1.80, 1.80
2 II (CH)	5.1	**23 II (CH_3)**	0.8	5.9	2.46, 2.51, 3.07
25 I (CH_3)	3.0	**25 I (CH_3)**	3.0	6.0	1.77, 1.78, 1.79
2 I (CH)	5.4	**23 II (CH_3)**	0.8	6.2	*2.44, 2.78, 3.12*
2 I (CH)	5.4	**23 I (CH_3)**	1.4	6.8	2.41, 2.48, 3.06
7a I (CH_2)	3.6	**7b I (CH_2)**	3.4	7.0	1.77
7a II (CH_2)	3.6	**7b II (CH_2)**	3.4	7.0	1.77
19 II (CH)	7.1	**25 II (CH_3)**	0.5	7.6	2.81, 3.42
2 II (CH)	5.1	**26 I (CH_3)**	2.8	7.9	*2.66, 2.67*
19 II (CH)	7.1	**23 II (CH_3)**	0.8	7.9	2.49
26 II (CH_3)	4.1	**26 II (CH_3)**	4.1	8.2	1.78, 1.79, 1.79
22 I (CH)	7.0	**23 I (CH_3)**	1.4	8.4	2.11, 3.31
19 I (CH)	7.2	**23 I (CH_3)**	1.4	8.6	2.61
19 I (CH)	7.2	**25 I (CH_3)**	3.0	10.2	2.91
30a II (NH_2)	7.0	**30b II (NH_2)**	4.0	11.0	1.76
19 II (CH)	7.1	**26 II (CH_3)**	4.1	11.2	2.93, 3.03
22 II (CH)	6.9	**21 II (CH)**	4.6	11.5	2.51
18 II (CH)	6.7	**2 II (CH)**	5.1	11.8	2.08
18 I (CH)	6.7	**2 I (CH)**	5.4	12.1	1.99
22 I (CH)	7.0	**21 I (CH)**	6.8	13.8	2.49
30a I (NH_2)	7.0	**30b I (NH_2)**	7.0	14.0	1.77
14 I (CH)	7.3	**30a II (NH_2)**	7.0	14.3	*2.89*
14 II (CH)	7.7	**30b I (NH_2)**	7.0	14.7	*3.16*

[a]Intermolecular proximities are denoted in italic font.

4. Discussion: Insight from NMR Crystallography into Hydrogen-Bonding and CH-π Interactions in Lorlatinib

A key focus of the application of NMR crystallography to the solid-state structure of Lorlatinib in this paper is on the key intermolecular hydrogen bonds formed by the NH_2 groups. Table 5 lists the N…N or N…O as well as H…N or H…O hydrogen bonding distances as well as the hydrogen-bonding angles for the hydrogen bonds formed by three of the four NH_2 hydrogen atoms (see Figure 2). Remember that, while there is only one NH_2 group in each Lorlatinib molecule, there are two distinct molecules in the asymmetric unit cell. Table 5 also lists the experimental and GIPAW calculated ^{1}H chemical shifts for these three NH_2 hydrogen atoms. As discussed in section 3.2.2, the discrepancy between experiment and GIPAW calculation is due to the temperature-dependence of ^{1}H chemical shifts for such hydrogen-bonded resonances. While the GIPAW calculation that effectively corresponds to 0 K shows a range of 1.5 ppm from 8.8 to 10.3 ppm for the three different NH_2 ^{1}H chemical shifts, it is curious that experimentally, no variation in the ^{1}H chemical shift, from 7.0 ppm is observed. Note that the ^{1}H chemical shift for the one of the four NH_2 protons that does not exhibit intermolecular hydrogen bonding is 4.0 ppm. It is further to be noted that the ^{14}N quadrupolar parameters are very similar for the two distinct NH_2 nitrogen sites, even though $N30^{I}$ exhibits an additional NH…O hydrogen bond. As shown in Table 3, the experimental quadrupolar product, P_Q, is the same, 3.4 MHz, with GIPAW calculation giving 3.3 and 3.6 MHz.

Table 5: Hydrogen bonding distances and angles[a] and experimental and GIPAW calculated ^{1}H chemical shifts for the NH_2 protons within Lorlatinib

Atom 1	Atom 2	Atom 3	Distance [1,3] (Å)	Distance [2,3] (Å)	Angle [1,2,3] (°)	Expt δ(^{1}H) (ppm)	Calc. δ(^{1}H) (ppm)
$N30^{II}$	$H30a^{II}$	$N15^{I}$	2.88	1.84	175.8	7.0	10.3
$N30^{I}$	$H30b^{I}$	$N15^{II}$	3.07	2.04	174.1	7.0	9.5
$N30^{I}$	$H30a^{I}$	$O2^{I}$	2.83	1.84	161.6	7.0	8.8

a (see also Figure 2)

An NMR crystallography analysis can also provide insight into CH-π interactions due to ring current interactions. As observed in the ^{1}H-^{13}C CP-HETCOR spectra presented in Figure 3 and discussed above in section 3.2.1, the ^{1}H chemical

shifts for the methyl hydrogens attached to C25 in the two distinct molecules in the asymmetric unit cell are significantly different, at 3.0 and 0.5 ppm. The much lower ^{1}H chemical shift of 0.5 ppm is explained by this methyl group pointing into the pyridine ring as shown in Figure 9.

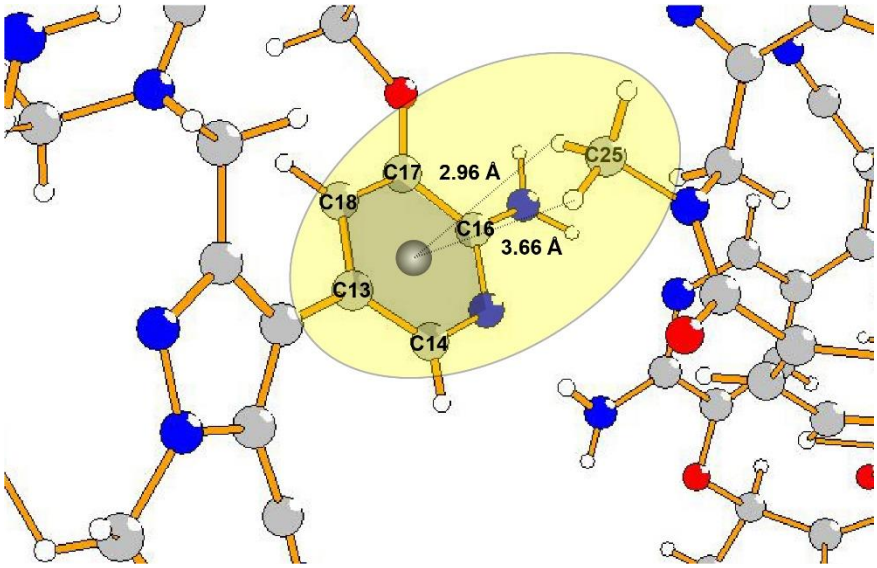

Figure 9: An intermolecular CH_3-π interaction between one of the C25 methyl groups and the pyridine ring of a neighbouring Lorlatinib molecule.

5. Summary and Outlook

This paper reports an analysis of the crystal structure of Lorlatinib, a treatment for non-small cell lung cancer, recognised as a 2021 ACS 'Hero of Chemistry. A NMR crystallography analysis that brings together X-ray diffraction, GIPAW calculation of NMR parameters and experimental multinuclear solid-state MAS NMR, including at 1 GHz, yields insight into the specific hydrogen-bonding interactions that drive the crystal packing. In particular, only three out of the four distinct NH_2 hydrogen atoms engage in intermolecular hydrogen bonding, as evidenced by a low ^{1}H chemical shift for one NH_2 hydrogen. Our work complements ongoing developments in the application of fast MAS to pharmaceuticals to show the power of NMR crystallography for characterising the solid-state forms of pharmaceutical molecules.[38,41,43,44,46,58,59,67,109]

Acknowledgements

Zainab Rehman thanks EPSRC and Pfizer for PhD funding. The UK High-Field Solid-State NMR Facility used in this research was funded by EPSRC and BBSRC (EP/T015063/1) and, for the 1 GHz instrument, EP/R029946/1. We thank Lucia Romero and Mateusz Pitak from Pharmorphix for single crystal X-ray diffraction data collection and structure determination. We acknowledge the X-ray diffraction Research Technology Platform at the University of Warwick for the PXRD experiments. The calculated and experimental data for this study are provided as a supporting data set from WRAP, the Warwick Research Archive Portal at http://wrap.warwick.ac.uk/***.

References

1. Syed YY. Lorlatinib: First Global Approval. *Drugs.* 2019; 79(1):93-98.
2. Nagasaka M, Ge Y, Sukari A, Kukreja G, Ou SI. A User's Guide to Lorlatinib. *Crit Rev Oncol Hematol* 2020; 151:102969.
3. Johnson TW, Richardson PF, Bailey S, Brooun A, B. J. Burke, Collins MR, Cui JJ, Deal JG, Deng Y, Dinh D, Engstrom LD, He M, Hoffman J, Hoffman RL, Huang Q, Kania RS, Kath JC, Lam H, Lam JL, Le PT, Lingardo L, Liu W, McTigue M, Palmer CL, Sach NW, Smeal T, Smith GL, Stewart AE, Timofeevski S, Zhu H, Zhu J, Zou HY, Edwards MP. Discovery of (10R)-7-Amino-12-fluoro-2,10,16-trimethyl-15-oxo-10,15,16,17-tetrahydro-2H-8,4-(metheno)pyrazolo[4,3-h][2,5,11]-benzoxadiazacyclotetradecine-3-carbonitrile (PF-06463922), a Macrocyclic Inhibitor of Anaplastic Lymphoma Kinase (ALK) and cros Oncogene 1 (ROS1) with Preclinical Brain Exposure and Broad-Spectrum Potency against ALK-Resistant Mutations. *J Med Chem.* 2014; 57:4720-4744.
4. Shaw AT, Felip E, Bauer TM, Besse B, Navarro A, Postel-Vinay S, Gainor JF, Johnson M, Dietrich J, James LP, Clancy JS, Chen J, Martini J, Abbattista A, Solomon BJ. Lorlatinib in non-small-cell lung cancer with ALK or ROS1 rearrangement: an international, multicentre, open-label, single-arm first-in-man phase 1 trial. *Lancet Oncol.* 2017; 18(12):1590-1599.
5. Solomon BJ, Besse B, Bauer TM, Felip E, Soo RA, Camidge DR, Chiari R, Bearz A, Lin C, Gadgeel SM, Riely GJ, Tan EH, Seto T, James LP, Clancy JS, Abbattista A, Martini J, Chen J, Peltz G, Thurm H, Ou SI, Shaw AT. Lorlatinib in patients with ALK-positive non-small-cell lung cancer: results from a global phase 2 study. *Lancet Oncol* 2018; 19(12):1654-1667.
6. ACS. *'Heroes of Chemistry' recognized for innovations in medicine*; September Washington, 2021. https://www.acs.org/content/acs/en/pressroom/newsreleases/2021/july/heroes-of-chemistry-recognized-for-innovations-in-medicine.htmlDOI: https://www.acs.org/content/acs/en/pressroom/newsreleases/2021/july/heroes-of-chemistry-recognized-for-innovations-in-medicine.html.

7. Taylor AA. *ACS celebrates its 2021 Heroes of Chemistry*; 44; 2021. https://cen.acs.org/people/awards/ACS-celebrates-its-2021-Heroes-of-Chemistry/99/i44DOI: https://cen.acs.org/people/awards/ACS-celebrates-its-2021-Heroes-of-Chemistry/99/i44.
8. *Lorviqua*; The Netherlands 2019. https://www.ema.europa.eu/en/documents/assessment-report/lorviqua-epar-public-assessment-report_en.pdfDOI: https://www.ema.europa.eu/en/documents/assessment-report/lorviqua-epar-public-assessment-report_en.pdf.
9. Ou X, Li X, Rong H, Yu L, Lu M. A general method for cultivating single crystals from melt microdroplets. *Chemical Communications.* 2020; 56(69):9950-9953.
10. Monti GA, Chattah AK, Linck YG. 2014. Chapter Four - Solid-State Nuclear Magnetic Resonance in Pharmaceutical Compounds. In Webb GA, editor Annual Reports on NMR Spectroscopy, ed., United Kingdom: Academic Press, Elsevier. p 221-269.
11. Berendt RT, Sperger DM, Isbester PK, Munson EJ. Solid-state NMR spectroscopy in pharmaceutical research and analysis. *Trends Anal Chem.* 2006; 25(10):977-984.
12. Li M, Xu W, Su Y. Solid-state NMR spectroscopy in pharmaceutical sciences *Trends Anal Chem.* 2021; 135:116152.
13. Nishiyama Y. Fast magic-angle sample spinning solid-state NMR at 60–100 kHz for natural abundance samples. *Solid State Nucl Magn Reson.* 2016; 78:24-36.
14. Sternberg U, Witter R, Kuprov I, Lamley JM, Oss A, Lewandowski JR, Samoson A. ^{1}H line width dependence on MAS speed in solid state NMR – Comparison of experiment and simulation. *J Magn Reson.* 2018; 291:32-39.
15. Yuan EC, Huang S, Huang H, Sinkkonen J, Oss A, Org M, Samoson A, Tai H, Chan JCC. Faster magic angle spinning reveals cellulose conformations in woods. *ChemComm.* 2021; 57:4110-4113.
16. Brown SP. Applications of high-resolution ^{1}H solid-state NMR. *Solid State Nucl Magn Res* 2012; 41:1-27.
17. Brown SP. Probing proton-proton proximities in the solid state. *Prog Nucl Magn Reson Spectrosc.* 2007; 50:199-251.
18. Sommer W, Gottwald J, Demco DE, Spiess HW. Dipolar Heteronuclear Multiple-Quantum NMR-Spectroscopy in Rotating Solids. *J Magn Reson Ser A.* 1995; 113(1):131-134.
19. Schnell I, Lupulescu A, Hafner S, Demco DE, Spiess HW. Resolution enhancement in multiple-quantum MAS NMR spectroscopy. *J Magn Reson* 1998; 133(1):61-69.
20. Saalwächter K, Graf R, Spiess HW. Recoupled Polarization Transfer Heteronuclear ^{1}H–^{13}C Multiple-Quantum Correlation in Solids under Ultra-fast MAS. *J Magn Reson* 1999; 140(2):471-476.
21. Ishii Y, Yesinowski JP, Tycko R. Sensitivity Enhancement in Solid-State ^{13}C NMR of Synthetic Polymers and Biopolymers by ^{1}H NMR Detection with High-Speed Magic Angle Spinning. *J Am Chem Soc.* 2001; 123(12):2921-2922.
22. Wiench JW, Bronnimann CE, Lin VS-Y, Pruski M. Chemical Shift Correlation NMR Spectroscopy with Indirect Detection in Fast Rotating Solids: Studies of Organically Functionalized Mesoporous Silicas. *J Am Chem Soc.* 2007; 129(40):12076-12077.
23. Zhou DH, Rienstra CM. Rapid analysis of organic compounds by proton-detected heteronuclear correlation NMR spectroscopy with 40 kHz magic-angle spinning. *Angew Chem Int Ed.* 2008; 47(38):7328-7331.
24. Nishiyama Y, Kobayashi T, Malon M, Singappuli-Arachchige D, Slowing II, Pruski M. Studies of minute quantities of natural abundance molecules using 2D heteronuclear

correlation spectroscopy under 100 kHz MAS. *Solid State Nucl Magn Reson.* 2015; 66-67:56-61.
25. Cavadini S. Indirect detection of nitrogen-14 in solid-state NMR spectroscopy. *Prog Nucl Magn Reson Spectrosc.* 2010; 56:46-77.
26. Cavadini S, Antonijevic S, Lupulescu A, Bodenhausen G. Indirect detection of nitrogen-14 in solids via protons by nuclear magnetic resonance spectroscopy. *J Magn Reson.* 2006; 182:168-178.
27. Tatton AS, Bradley JP, Iuga D, Brown SP. ^{14}N–^{1}H Heteronuclear Multiple-Quantum Correlation Magic-Angle Spinning NMR Spectroscopy of Organic Solids. *Z Phys Chem.* 2012; 226:1187-1203.
28. Gan ZH, Amoureux JP, Trebosc J. Proton-detected ^{14}N MAS NMR using homonuclear decoupled rotary resonance. *Chem Phys Lett.* 2007; 435:163-169.
29. Leclaire J, Poisson G, Ziarelli F, Pepe G, Fotiadu F, Paruzzo FM, Rossini AJ, Dumez J, Elena-Herrmann B, Emsley L. Structure elucidation of a complex CO_2-based organic framework material by NMR crystallography. *Chem Sci.* 2016; 7:4379-4390.
30. Guzmán-Afonso C, Hong Y, Colaux H, Iijima H, Saitow A, Fukumura T, Aoyama Y, Motoki S, Oikawa T, Yamazaki T, Yonekura K, Nishiyama Y. Understanding hydrogen-bonding structures of molecular crystals via electron and NMR nanocrystallography. *Nat Commun.* 2019; 10:3537.
31. Corlett EK, Blade H, Hughes LP, Sidebottom PJ, Walker D, Walton RI, Brown SP. An XRD and NMR crystallographic investigation of the structure of 2,6-lutidinium hydrogen fumarate. *CrystEngComm.* 2019; 21(22):3502-3516.
32. Hofstetter A, Balodis M, Paruzzo FM, Widdifield CM, Steyanato G, Pinon AC, Bygrave PJ, Day GM, Emsley L. Rapid Structure Determination of Molecular Solids Using Chemical Shifts Directed by Unambiguous Prior Constraints. *J Am Chem Soc.* 2019; 141(42):16624-16634.
33. Hong Y, Reddy GNM, Nishiyama Y. Selective detection of active pharmaceutical ingredients in tablet formulations using solid-state NMR spectroscopy. *Solid State Nucl Magn Reson.* 2020; 106:101651.
34. Venâncio T, Oliveira LM, Ellena J, Boechat N, Brown SP. Probing intermolecular interactions in a diethylcarbamazine citrate salt by fast MAS ^{1}H solid-state NMR soectroscopy and GIPAW calculations. *Solid State Nucl Magn Reson.* 2017; 87:73-79.
35. Pawlak T, Sudgen I, Bujacz G, Iuga D, Brown SP, Potrzebowski MJ. Synergy of Solid-State NMR, Single-Crystal X-ray Diffraction, and Crystal Structure Prediction Methods: A Case Study of Teriflunomide (TFM). *Cryst Growth Des.* 2021; 21(6):3328-3343.
36. Lu X, Xu W, Hanada M, Jermain SV, WilliamsIII RO, Su Y. Solid-State NMR analysis of crystalline and amorphous Indomethacin: An experimental protocol for full resonance assignments. *J Pharm Biomed Anal.* 2019; 165:47-55.
37. Fenniri H, Tikhomirov GA, Brouwer DH, Bouatra S, Bakkari ME, Yan Z, Cho J, Yamazaki T. High Field Solid-State NMR Spectroscopy Investigation of $^{(15)}N$-Labeled Rosette Nanotubes: Hydrogen Bond Network and Channel-Bound Water. *J Am Chem Soc.* 2016; 138(19):6115-6118.
38. Dudek MK, Śniechowska J, Wróblewska A, Kaźmierski S, Potrzebowski MJ. Cocrystals "Divorce and Marriage": When a Binary System Meets an Active Multifunctional Synthon in a Ball Mill. *Chem Eur J.* 2020; 26(58):13264-13273.

39. Reddy GNM, Huqi A, Iuga D, Sakurai S, Marsh A, Davis JT, Masiero S, Brown SP. Co-existence of Distinct Supramolecular Assemblies in Solution and in the Solid State. *Chem Eur J.* 2016; 23(10):2315-2322.
40. Zhang R, Hong Y, Ravulaa T, Nishiyama Y, Ramamoorthy A. High-resolution proton-detected MAS experiments on self-assembled diphenylalanine nanotubes enabled by fast MAS and high magnetic field. *J Magn Reson* 2020; 313:106717.
41. Hirsh DA, Wijesekara AV, Carnahan SL, Hung I, Lubach JW, Nagapudi K, Rossini AJ. Rapid Characterization of Formulated Pharmaceuticals Using Fast MAS ^{1}H Solid-State NMR Spectroscopy. *Mol Pharm.* 2019; 16(7):3121-3132.
42. Jain MG, Mote KR, Madhu PK. NMR Crystallography at Fast Magic-Angle Spinning Frequencies: Application of Novel Recoupling Methods. *Crystals.* 2019; 9:231.
43. Pugliese A, Toresco M, McNamara D, Iuga D, Abraham A, Tobyn M, Hawarden LE, Blanc F. Drug–Polymer Interactions in Acetaminophen/Hydroxypropylmethylcellulose Acetyl Succinate Amorphous Solid Dispersions Revealed by Multidimensional Multinuclear Solid-State NMR Spectroscopy. *Mol Pharm.* 2021; 18:3519-3531.
44. Grüne M, Luxenhofer R, Iuga D, Brown SP, Pöppler A. ^{14}N–^{1}H HMQC solid-state NMR as a powerful tool to study amorphous formulations – an exemplary study of paclitaxel loaded polymer micelles. *J Mater Chem B.* 2020; 8:6827-6836.
45. Bártová K, Císařová I, Lyčka A, Dračínský M. Tautomerism of azo dyes in the solid state studied by ^{15}N, ^{14}N, ^{13}C and ^{1}H NMR spectroscopy, X-ray diffraction and quantum-chemical calculations. *Dyes Pigm.* 2020; 178:108342.
46. Lu X, Skomski D, Thompson KC, McNevin MJ, Xu W, Su Y. Three-Dimensional NMR Spectroscopy of Fluorinated Pharmaceutical Solids under Ultrafast Magic Angle Spinning. *Anal Chem* 2019; 91:6217-6224.
47. Quinn CM, Zadorozhnyi R, Struppe J, Sergeyev IV, Gronenborn AM, Polenova T. Fast ^{19}F Magic-Angle Spinning Nuclear Magnetic Resonance for the Structural Characterization of Active Pharmaceutical Ingredients in Blockbuster Drugs. *Anal Chem.* 2021; 93:13029-13037.
48. Hodgkinson P. NMR Crystallography of molecular organics. *Prog Nucl Magn Reson Spectrosc.* 2020; 118-119:10-53.
49. Bryce DL. NMR crystallography: structure and properties of materials from solid-state nuclear magnetic resonance observables. *IUCrJ.* 2017; 4:350-359.
50. Harris RK. Applications of solid-state NMR to pharmaceutical polymorphism and related matters. *J Pharm Pharmacol* 2006; 59(2):225-239.
51. Harris RK. NMR Crystallography: the use of chemical shifts. *Solid State Sci.* 2004; 6(10):1025-1037.
52. Ashbrook SE, McKay D. Combining solid-state NMR spectroscopy with first-principles calculations – a guide to NMR crystallography. *ChemComm.* 2016; 52:7186-7204.
53. Beran GJO, Hartman JD, Heit YN. Predicting Molecular Crystal Properties from First Principles: Finite Temperature Thermochemistry to NMR Crystallography. *Acc Chem Res.* 2016; 49(11):2501-2508.
54. Charpentier T. The PAW/GIPAW approach for computing NMR parameters: A new dimension added to NMR study of solids. *Solid State Nucl Magn Reson.* 2011; 40(1):1-20.
55. Bonhomme C, Gervais C, Babonneau F, Coelho C, Pourpoint F, Azaïs T, Ashbrook SE, Griffin JM, Yates JR, Mauri F, Pickard CJ. First-Principles Calculation of NMR Parameters Using the Gauge Including Projector Augmented Wave Method: A Chemist's Point of View. *Chem Rev.* 2012; 112(11):5733-5779.

56. Pickard CJ, Mauri F. All-electron magnetic response with pseudopotentials: NMR chemical shifts. *Phys Rev B* 2001; 63:245101.
57. Yates JR, Pickard CJ, Mauri F. Calculation of NMR chemical shifts for extended systems using ultrasoft pseudopotentials. *Phys Rev B* 2007; 76:024401.
58. Szell PMJ, Brown SP, Hughes LP, Blade H, Nilsson-Lill SO. A curious case of dynamic disorder in pyrrolidine rings elucidated by NMR crystallography. *ChemComm.* 2020; 56(90):14039-14042.
59. Szell PMJ, Lewandowski JR, Blade H, Hughes LP, Nilsson-Lill SO, Brown SP. Taming the dynamics in a pharmaceutical by cocrystallization: investigating the impact of the coformer by solid-state NMR. *CrystEngComm.* 2021; 23:6859-6870.
60. Kerr HE, Softley LK, Suresh K, Hodgkinson P, Evans IR. Structure and physicochemical characterization of a naproxen–picolinamide cocrystal. *Acta Crystallogr C Struct Chem.* 2017; 1(73):168-175.
61. Stevens JS, Byard SJ, Muryn CA, Schroeder SL. Identification of protonation state by XPS, solid-state NMR, and DFT: characterization of the nature of a new theophylline complex by experimental and computational methods. *J Phys Chem B.* 2010; 114:13961 - 13969.
62. Stevens JS, Byard SJ, Schroeder SL. Salt or co-crystal? Determination of protonation state by X-ray photoelectron spectroscopy (XPS). *J Pharm Sci.* 2010; 99:4453 - 4457.
63. Tatton AS, Blade H, Brown SP, Hodgkinson P, Hughes LP, Nilsson-Lill SO, Yates JR. Improving Confidence in Crystal Structure Solutions Using NMR Crystallography: The Case of β-Piroxicam. *Cryst Growth Des.* 2018; 18:3339-3351.
64. Cordova M, Balodis M, de Almeida BS, Ceriotti M, Emsley L. Bayesian probabilistic assignment of chemical shifts in organic solids. *Sci Adv.* 2021; 7(48):1-10.
65. Paruzzo FM, Hofstetter A, Musil F, De S, Ceriotti M, Emsley L. Chemical shifts in molecular solids by machine learning. *Nat Commun.* 2018; 9(4501):4501.
66. Engel EA, Anelli A, Hofstetter A, Paruzzo F, Emsley L, Ceriotti M. A Bayesian approach to NMR crystal structure determination. *Phys Chem Chem Phys.* 2019; 21(42):23385-23400.
67. Cordova M, Balodis M, Hofstetter A, Paruzzo F, Nilsson-Lill SO, Eriksson ESE, Berruyer P, de Almeida BS, Quayle MJ, Norberg ST, Ankarberg AS, Schantz S, Emsley L. Structure determination of an amorphous drug through large-scale NMR predictions. *Nat Commun.* 2021; 12:2964.
68. Reif B, Ashbrook SE, Emsley L, Hong M. Solid-State NMR Spectroscopy *Nat Rev Methods Primers.* 2021; 1:1-22.
69. Pencheva KD, Birch MJ, McAllister M, Rowland M, Smales IL. *Crystalline form of lorlatinib free base*; 16751665.7; 2019. DOI: https://patents.google.com/patent/US20190365712A1/en.
70. Sheldrick GM. A short history of SHELX. *Acta Crystallogr A.* 2008; 64:112-122.
71. Macrae CF, Edgington PR, McCabe P, Pidcock E, Sheilds GP, Taylor R, Towler M, van de Streek J. Mercury: Visualisation and Analysis of Crystal Structures. *J Appl Crystallogr.* 2006; 39:453-457.
72. Shaka AJ, Keeler J, Frenkiel T, Freeman R. An improved sequence for broadband decoupling: WALTZ-16. *J Magn Reson.* 1983; 52(2):335-338.
73. Metz G, Wu X, Smith SO. Ramped-Amplitude Cross Polarization in Magic-Angle-Spinning NMR. *J Magn Reson A.* 1994; 1994(2):219-227.
74. Meier BH. Cross polarization under fast magic angle spinning—thermodynamical considerations. *Chem Phys Lett.* 1992; 188:201-207.

75. Laage S, R.Sachleben J, Steuernagel S, Pierattelli R, Pintacuda G, Emsley L. Fast acquisition of multi-dimensional spectra in solid-state NMR enabled by ultra-fast MAS. *J Magn Reson.* 2009; 196(2):133-141.
76. Fung BM, Khitrin AK, Ermolaev K. An improved broadband decoupling sequence for liquid crystals and solids. *J Magn Reson.* 2000; 142(1):97-101.
77. Ernst M, Meier MA, Tuherm T, Samoson A, Meier BH. Low-Power High-Resolution Solid-State NMR of Peptides and Proteins. *J Am Chem Soc.* 2004; 126(15):4764-4765.
78. Bielecki A, Kolbert AC, Levitt MH. Frequency-switched pulse sequences: Homonuclear decoupling and dilute spin NMR in solids. *Chem Phys Lett.* 1989; 155(4-5):341-346.
79. Levitt MH, Oas TG, Griffin RG. Rotary Resonance Recoupling in Heteronuclear Spin Pair Systems. *Isr J Chem* 1988; 28:271-282.
80. Oas TG, Griffin RG, Levitt MH. Rotary resonance recoupling of dipolar interactions in solid-state nuclear magnetic resonance spectroscopy. *J Chem Phys.* 1988; 89:692-695.
81. Costa PR, Gross JD, Hong M, Griffin RG. *Chem Phys Lett.* 1997; 280:95.
82. Webber AL, Masiero S, Pieraccini S, Burley JC, Tatton AS, Iuga D, Pham TN, Spada GP, Brown SP. Identifying Guanosine Self Assembly at Natural Isotopic Abundance by High-Resolution ^{1}H and ^{13}C Solid-State NMR Spectroscopy. *J Am Chem Soc.* 2011; 133:19777–19795.
83. Huang S-J, Liu S-B, Chan JCC. Heteronuclear dipolar recoupling of half-integer quadrupole nuclei under fast magic angle spinning. *Solid State Nuclear Magnetic Resonance.* 2009; 36(2):110-117.
84. Hayashi S, Hayamizu K. Chemical Shift Standards in High-Resolution Solid-State NMR (1) ^{13}C, ^{29}Si, and ^{1}H Nuclei. *Bull Chem Soc Jpn.* 1991; 64:685-687.
85. Morcombe CR, Zilm KW. Chemical shift referencing in MAS solid state NMR. *J Magn Reson.* 2003; 162(2):479-486.
86. Hayashi S, Hayamizu K. Chemical Shift Standards in High-Resolution Solid-State NMR (2)^{15}N Nuclei. *Bull Chem Soc Jpn.* 1991; 64:688-690.
87. Harris RK, Becker ED, Menezes SMCD, Granger P, Hoffman RE, Zilm KW. Further Conventions for NMR Shielding and Chemical Shifts (IUPAC Recommendations 2008). *Magn Reson Chem.* 2008; 46:582-598.
88. Martin GE, Hadden CE. Long-Range ^{1}H-^{15}N Heteronuclear Shift Correlation at Natural Abundance. *J Nat Prod.* 2000; 63:543-585.
89. Clark SJ, Segall MD, Pickard CJ, Hasnip PJ, Probert MJ, Refson K, Payne MC. First principles methods using CASTEP. *Z Kristallogr.* 2005; 220:567-570.
90. Perdew JP, Burke K, Ernzerhof M. Generalized Gradient Approximation Made Simple. *Phys Rev Lett.* 1996; 77:3865-3868.
91. Hartman JD, Kudla RA, Day GM, Mueller LJ, Beran GJO. Benchmark fragment-based ^{1}H, ^{13}C, ^{15}N and ^{17}O chemical shift predictions in molecular crystals. *Phys Chem Chem Phys.* 2016; 18:21686 - 21709.
92. Webber AL, Emsley L, Claramunt RM, Brown SP. NMR Crystallography of Campho[2,3-c]pyrazole (Z′ = 6): Combining High-Resolution ^{1}H-^{13}C Solid-State MAS NMR Spectroscopy and GIPAW Chemical-Shift Calculations. *J Phys Chem A.* 2010; 114(38):10435-10442.
93. Brown SP. 2018. *Modern Methods in Solid-State NMR: A Practitioner's Guide*. 1st ed., Cambridge: Royal Society of Chemistry.High-resolution ^{1}H 2D Magic-angle Spinning Techniques for Organic Solids. Hodgkinson P. p 39-74.

94. Harris RK, Hodgkinson P, Pickard CJ, Yates JR, Zorin V. Chemical shift computations on a crystallographic basis: some reflections and comments. *Magn Reson Chem.* 2007; 45:S174-S186.
95. Corlett EK, Blade H, Hughes LP, Sidebottom PJ, Walker D, Walton RI, Brown SP. Investigating discrepancies between experimental solid-state NMR and GIPAW calculation: NC–N ^{13}C and OH···O ^{1}H chemical shifts in pyridinium fumarates and their cocrystals. *Solid State Nucl Magn Reson.* 2020; 108:101662.
96. Harris RK. NMR studies of organic polymorphs & solvates. *Analyst.* 2006; 131(3):351-373.
97. Reddy GNM, Cook DS, Iuga D, Walton RI, Marsh A, Brown SP. An NMR crystallography study of the hemihydrate of 2 ', 3 '-O-isopropylidineguanosine. *Solid State Nucl Magn Reson.* 2015; 65:41-48.
98. Tatton AS, Pham TN, Vogt FG, Iuga D, Edwards AJ, Brown SP. Probing Hydrogen Bonding in Cocrystals and Amorphous Dispersions Using ^{14}N-^{1}H HMQC Solid-State NMR. *Mol Pharm* 2013; 10:999-1007.
99. Liddel U, Ramsey NF. Temperature Dependent Magnetic Shielding in Ethyl Alcohol. *J Chem Phys.* 1951; 19:1608-1608.
100. Arnold JT, Packard ME. Variations in Absolute Chemical Shift of Nuclear Induction Signals of Hydroxyl Groups of Methyl and Ethyl Alcohol. *J Chem Phys.* 1951; 19:1608-1609.
101. Muller N, Reiter RC. Temperature Dependence of Chemical Shifts of Protons in Hydrogen Bonds. *J Chem Phys.* 1965; 42:3265-3269.
102. Garcia-Viloca M, Gelabert R, González-Lafont À, Moreno M, Lluch JM. Temperature Dependence of Proton NMR Chemical Shift As a Criterion To Identify Low-Barrier Hydrogen Bonds. *J Am Chem Soc.* 1998; 120:10203-10209.
103. Sośnicki JG, Hansen PE. Temperature Coefficient of NH Chemical Shifts of Thioamides and Amides in Relation to Structure. *J Mol Struct.* 2004; 700:91-103.
104. Brown SP, Schnell I, Brand JD, Mullen K, Spiess HW. The competing effects of π–π packing and hydrogen bonding in a hexabenzocoronene carboxylic acid derivative: A ^{1}H solid-state MAS NMR investigation. *Phys Chem Chem Phys* 2000; 2:1735-1745.
105. Webber AL, Elena B, Griffin JM, Yates JR, Pham TN, Mauri F, Pickard CJ, Gil AM, Stein R, Lesage A, Emsley L, Brown SP. Complete ^{1}H resonance assignment of β-maltose from ^{1}H–^{1}H DQ-SQ CRAMPS and ^{1}H (DQ-DUMBO)–^{13}C SQ refocused INEPT 2D solid-state NMR spectra and first principles GIPAW calculations. *Phys Chem Chem Phys.* 2010; 12:6970-6983.
106. Mann SK, Devgan MK, Franks WT, Huband S, Chan CL, Griffith J, Pugh D, Brooks NJ, Welton T, Pham TN, McQueen LL, Lewandowski JR, Brown SP. MAS NMR Investigation of Molecular Order in an Ionic Liquid Crystal. *J Phys Chem B.* 2020; 124(24):4975-4988.
107. Štoček JR, Socha O, Císařová I, Slanina T, Dračínský M. Importance of Nuclear Quantum Effects for Molecular Cocrystals with Short Hydrogen Bonds. *Journal of the American Chemical Society.* 2022; 144(16):7111-7116.
108. Dumez JN, Pickard CJ. Calculation of NMR chemical shifts in organic solids: Accounting for motional effects. *J Chem Phys.* 2009; 130:104701.
109. Struppe J, Quinn CM, Sarkar S, Gronenborn AM, Polenova T. Ultrafast ^{1}H MAS NMR Crystallography For Natural Abundance Pharmaceutical Compounds. *Mol Pharm.* 2020; 17:674-682.